

# *Relationship between the AMOC and the multidecadal variability of the midlatitude southern Indian Ocean*

Article

Published Version

Creative Commons: Attribution 4.0 (CC-BY)

Open Access

Zhang, R., Dong, B. ORCID: <https://orcid.org/0000-0003-0809-7911>, Wen, Z., Guo, Y. and Chen, X. (2023) Relationship between the AMOC and the multidecadal variability of the midlatitude southern Indian Ocean. *Journal of Climate*, 36 (24). pp. 8761-8781. ISSN 1520-0442 doi: 10.1175/JCLI-D-23-0198.1 Available at <https://centaur.reading.ac.uk/114183/>

It is advisable to refer to the publisher's version if you intend to cite from the work. See [Guidance on citing](#).

To link to this article DOI: <http://dx.doi.org/10.1175/JCLI-D-23-0198.1>

Publisher: American Meteorological Society

All outputs in CentAUR are protected by Intellectual Property Rights law, including copyright law. Copyright and IPR is retained by the creators or other copyright holders. Terms and conditions for use of this material are defined in the [End User Agreement](#).

[www.reading.ac.uk/centaur](http://www.reading.ac.uk/centaur)

**CentAUR**

Central Archive at the University of Reading

Reading's research outputs online

## Relationship between the AMOC and the Multidecadal Variability of the Midlatitude Southern Indian Ocean

RUIJIE ZHANG,<sup>a,b</sup> BUWEN DONG,<sup>b</sup> ZHIPING WEN,<sup>a,c,d,e</sup> YUANYUAN GUO,<sup>a</sup> AND XIAODAN CHEN<sup>a</sup>

<sup>a</sup> *Department of Atmospheric and Oceanic Sciences and Institute of Atmospheric Sciences, Fudan University, Shanghai, China*

<sup>b</sup> *National Centre for Atmospheric Science, Department of Meteorology, University of Reading, Reading, United Kingdom*

<sup>c</sup> *Shanghai Key Laboratory of Ocean–Land–Atmosphere Boundary Dynamics and Climate Change, Fudan University, Shanghai, China*

<sup>d</sup> *Institute of Eco-Chongming (IEC), Chongming, Shanghai, China*

<sup>e</sup> *Jiangsu Collaborative Innovation Center for Climate Change, China*

(Manuscript received 4 April 2023, in final form 5 August 2023, accepted 28 September 2023)

**ABSTRACT:** Air–sea coupling system in the southwestern Indian Ocean (SWIO; 35°–55°S, 40°–75°E) exhibits predominant multidecadal variability that is the strongest during austral summer. It is characterized by an equivalent barotropic atmospheric high (low) pressure over warm (cold) sea surface temperature (SST) anomalies and a poleward (equatorward) shift of the westerlies during the positive (negative) phase. In this study, physical processes of this multidecadal variability are investigated by using observations/reanalysis and CMIP6 model simulations. Results suggest that the multidecadal fluctuation can be explained by the modulation of the Atlantic meridional overturning circulation (AMOC) and the local air–sea positive feedback in the SWIO. In both observations/reanalysis and CMIP6 model simulations, the AMOC fluctuation presents a significantly negative correlation with the multidecadal SST variation in the SWIO when the AMOC is leading by about a decade. The mechanisms are that the preceding AMOC variation can cause an interhemispheric dipolar pattern of SST anomalies in the Atlantic Ocean. Subsequently, the SST anomalies in the midlatitudes of the South Atlantic can propagate to the SWIO by the oceanic Rossby wave under the influence of the Antarctic Circumpolar Current (ACC). Once the SST anomalies reach the SWIO, these SST anomalies in the oceanic front can affect the baroclinicity in the lower troposphere to influence the synoptic transient eddy and then cause the atmospheric circulation anomaly via the eddy–mean flow interaction. Subsequently, the anomalous atmospheric circulation over the SWIO can significantly strengthen the SST anomalies through modifying the oceanic meridional temperature advection and latent and sensible heat flux.

**KEYWORDS:** Indian Ocean; Southern Ocean; Atmosphere–ocean interaction; Meridional overturning circulation; Multidecadal variability

### 1. Introduction

Understanding low-frequency climate variability is a key issue in projecting future climate change and is a major challenge for the climate research community. Many observational studies detected midlatitude climate variability on the decadal to multidecadal time scale in the Northern Hemisphere, such as the Pacific decadal oscillation (PDO) in the North Pacific and the Atlantic multidecadal oscillation (AMO) in the North Atlantic (NA; Wallace and Jiang 1987; Kerr 2000). Although some studies discussed low-frequency variability in southern Africa, Australia, and the Southern Ocean (Power et al. 1999; Hogg and Blundell 2006; Jury 2015), low-frequency climate variability in the midlatitude Southern Hemisphere is still less understood.

Some studies implied the possible existence of decadal variability in austral summer of sea surface temperature (SST)

and atmospheric circulation pattern over the southern Indian Ocean (SIO), particularly the Agulhas Current, retroflection, and outflow zones in the southwestern Indian Ocean (Allan et al. 1995; Reason et al. 1996; Reason and Lutjeharms 1998). The Agulhas Current is the strongest western boundary current in the Southern Hemisphere (Reason 2001; Rouault et al. 2003), where the oceanic front and storm track are intense and the air–sea interaction is active (Rouault et al. 2002; Nakamura et al. 2008; Nonaka et al. 2009). The low-frequency variability of SST and atmosphere in the SIO can range from a decadal to multidecadal time scale, characterized by an equivalent barotropic low (high) over a cold (warm) oceanic surface (Allan et al. 1995; Reason et al. 1996; Reason and Lutjeharms 1998; Morioka et al. 2015a; Zhang et al. 2021), and can notably influence the low-frequency precipitation variation in southern Africa and Australia (Power et al. 1999; Malherbe et al. 2014; Jury 2015).

The low-frequency climate variation of the SIO can arise from external forcing exerted by volcanoes and the Antarctic ozone hole or internal variability (Thompson et al. 2011; Gao et al. 2023). For internal variability, substantial observations and model simulations have proved that the midlatitude air–sea positive feedback is a potential source (Latif and Barnett 1994; Miller and Schneider 2000; Zhong et al. 2008; Fang and Yang 2011, 2016). The atmospheric anomalies mainly impact the midlatitude ocean through the air–sea heat flux and

Denotes content that is immediately available upon publication as open access.

Supplemental information related to this paper is available at the Journals Online website: <https://doi.org/10.1175/JCLI-D-23-0198.s1>.

Corresponding author: Zhiping Wen, [zpwen@fudan.edu.cn](mailto:zpwen@fudan.edu.cn)

DOI: 10.1175/JCLI-D-23-0198.1

© 2023 American Meteorological Society. This published article is licensed under the terms of a Creative Commons Attribution 4.0 International (CC BY 4.0) License



upper-ocean current induced by surface wind stress (Cayan 1992; Seager et al. 2001; R. Zhang et al. 2020). Changes in SST, particularly in the midlatitude oceanic frontal zones, where the tropospheric baroclinicity is strong, may influence the transient eddy activities to reinforce the atmospheric anomalies through the eddy–mean flow interaction (Liu and Wu 2004; Zhong et al. 2008; Fang and Yang 2011, 2016; Chen et al. 2020). This mechanism has been demonstrated to be one of the important processes responsible for the decadal SST variability in the North Pacific and North Atlantic. (Latif and Barnett 1994; Kushnir et al. 2002; Zhong et al. 2008; Fang and Yang 2016). However, the features of the local air–sea positive feedback and its potential impact on the SIO are still not fully revealed.

Moreover, some remote forcings from the Pacific and Atlantic can also influence the low-frequency SST variability in the SIO (Reason et al. 1996; Morioka et al. 2015a, 2017; Le Bars et al. 2016; Xue et al. 2018a,b). The climate variability in the Pacific can affect the SST anomaly in the SIO by changing the Indonesian throughflow on the decadal time scale (Reason et al. 1996; Liu et al. 2015; Y. Zhang et al. 2018). Xue et al. (2018a,b) mentioned that the South Atlantic (SA) multidecadal SST anomalies can impact the multidecadal fluctuations in the SIO through an atmospheric bridge mechanism or triggering an eastward propagating South Atlantic–Australia (SAA) wave train. Additionally, the decadal SST and SLP anomalies slowly propagating eastward from the SA can influence the oceanic and atmospheric patterns in the SIO as well (Morioka et al. 2015a, 2017).

As an important multidecadal component of the global climate system, the Atlantic meridional overturning circulation (AMOC) has a marked effect on the multidecadal variation in both the Northern and Southern Hemispheres (Buckley and Marshall 2016; Zhang et al. 2019). The AMOC variation can influence the subtropical high in the SA via atmospheric teleconnection (Orihuela-Pinto et al. 2022). Besides, the AMOC can also result in extended regions of pronounced seesaw structure of the SST anomalies in the Atlantic Ocean by influencing the meridional oceanic heat transport. The positive phase of the AMOC is associated with enhanced northward heat transport and therefore leads to the negative (positive) SST anomaly in the midlatitudes of the SA (NA) (Venzke et al. 2000; Vellinga and Wood 2002; Latif et al. 2004, 2006; Dima and Lohmann 2010; Sun et al. 2013, 2018). Considering the significant influence of the AMOC on the climate variability in the SA, as well as the impact of the multidecadal anomalies in the SA on the SIO region, a linkage might exist between the AMOC fluctuations and the low-frequency variability of the SIO. However, few studies have addressed this issue. The exact relationship between the AMOC and the climate anomalies in the SIO is still unclear, and the possible physical processes by which the AMOC affects the SIO also require further exploration.

The purpose of this paper is to investigate the characteristics of the low-frequency variability of the SIO and to explore the possible role of the AMOC in influencing the SIO. Meanwhile, the features and effects of the local air–sea positive feedback on the low-frequency variability of the SIO will also

be examined in the present study. The rest of the paper is organized as follows. Datasets, models, and methods used in this study are described in section 2. In section 3, the characteristics of the low-frequency variability of the SIO are presented. Section 4 attempts to investigate the possible impact of the AMOC fluctuation on the SIO based on observations/reanalysis and CMIP6 model simulations. Section 5 mainly discusses the local air–sea positive feedback processes and their role in maintaining the low-frequency anomalies in the SIO. The discussion and conclusions are presented in sections 6 and 7.

## 2. Datasets, models, and methods

### a. Datasets and models

The datasets used in this study consist of 1) monthly mean SST of National Oceanic and Atmospheric Administration (NOAA) Extended Reconstructed SST dataset version 5 from 1870 to 2020 with a resolution of  $2.5^\circ$  (ERSST5; Huang et al. 2017); 2) monthly mean atmospheric fields with a horizontal resolution of  $0.5^\circ$  taken from the fifth-generation European Centre for Medium-Range Weather Forecasts (ECMWF) atmospheric reanalysis (ERA5) from 1950 to 2020, including sea level pressure, 10-m horizontal winds, surface heat flux, net surface radiation, geopotential height, horizontal wind, and air temperature from 1000 to 100 hPa (Bell et al. 2020; Hersbach et al. 2019a,b); 3) daily horizontal winds and air temperature from 1000 to 200 hPa with a  $1^\circ \times 1^\circ$  grid of ERA5 from 1950 to 2020 (Hersbach et al. 2018); 4) monthly mean oceanic temperature and zonal current of the University of Maryland (UMD) Simple Ocean Data Assimilation Reanalysis Version 2.2.4 (SODA 2.2.4) from 1950 to 2010 with a resolution of  $0.5^\circ$  (Carton et al. 2005; Carton and Giese 2008); 5) monthly mean oceanic mixed layer depth of NCEP Global Ocean Data Assimilation System (GODAS) from 1980 to 2020 (Behringer et al. 1998); and 6) AMOC streamfunction profiles from the RAPID array across the Atlantic at  $26^\circ\text{N}$  since 2004 (Rayner et al. 2011).

To address the question of what the relationship between AMOC and the low-frequency signal in the SIO is, the monthly outputs of preindustrial control (piControl) simulations from 10 models from phase 6 of the Coupled Model Intercomparison Project (CMIP6; Eyring et al. 2016) are examined in the present study (Table 1). The duration of each model simulation is 450 years, except for GISS-E2-1-G (344 years). For ease of analysis, the monthly SST and sea surface height (SSH) of each model simulation are remapped onto a  $1^\circ \times 1^\circ$  regular grid. Since the role of external forcing is not the focus of the present study, the long-term linear trend in all observational and model variables is removed.

### b. Methods

The two-tailed Student's *t* test was used to determine the significance levels of linear regression. To consider the influence of autocorrelation on degrees of freedom, the effective

TABLE 1. Correlation coefficients between AMOC\_SF, AMOC\_SST, and SST in the SA pole and NA pole on the multidecadal time scale (>30 years). The period shorter than 17 years was removed to extract the multidecadal time scale in the ACCESS-CM2, FGOALS-g3, and GISS-E2-1-G, in which the multidecadal period of the AMOC is shorter compared with other models. The numbers in parentheses represent the lagging years of AMOC\_SST when the correlation between AMOC\_SF and AMOC\_SST reaches the maximum. Asterisks (\*) indicate the correlation exceeding the 90% confidence level.

Model	AMOC_SST		
	index	SA pole	NA pole
ACCESS-CM2	0.54 (5)*	0.19	0.65*
ACCESS-ESM1-5	0.55 (15)*	-0.16	0.63*
CanESM5	0.06 (10)	-0.17	-0.03
CESM2	0.80 (7)*	-0.01	0.88*
FGOALS-g3	0.85 (2)*	0.14	0.88*
GFDL-CM4	0.54 (3)*	-0.29	0.65*
GISS-E2-1-G	0.40 (9)*	-0.17	0.40*
HadGEM3-GC3.1-LL	0.75 (2)*	-0.48*	0.68*
MIROC6	0.76 (1)*	-0.27	0.76*
MRI-ESM2-0	0.77 (3)*	0.29	0.85 (3)*

number of degrees of freedom can be given by the following approximation:

$$\frac{1}{N_{\text{eff}}} \approx \frac{1}{N} + \frac{2}{N} \sum_{j=1}^N \frac{N-j}{N} \rho_{xx}(j)\rho_{yy}(j), \quad (1)$$

in which  $N$  is the sample size, and  $\rho_{xx}$  and  $\rho_{yy}$  represent the autocorrelations of time series  $x$  and  $y$  at time lag  $j$ . In the

present study, two different AMOC indices are used. Due to the lack of long-term observational data on the AMOC, a dipole index based on the annual mean SST difference between the midlatitude North Atlantic (NA pole; 40°–60°N, 60°–10°W) and the South Atlantic (SA pole; 40°–60°S, 50°W–0°) is constructed to represent the AMOC index in observations (Latif et al. 2006) and it is referred to as AMOC\_SST, which has good consistency with the observational AMOC from the RAPID since 2004–20 on a decadal time scale (not shown). Additionally, we used the annual mean meridional overturning streamfunction averaged from 20° to 30°N at a depth of 1000 m in the Atlantic Ocean to construct another AMOC index that is referred to as AMOC\_SF. The AMOC\_SST and AMOC\_SF have a good relationship in the CMIP6 models that we utilized, except for CanESM5 (Table 1).

### 3. Features of the multidecadal variability of the southern Indian Ocean

The spatial distributions of the low-frequency SST variances for different seasons in observations are illustrated in Fig. 1. They reveal obvious decadal (>8 years) and multidecadal variances (>17 years) in all four seasons to the south of Madagascar where the Agulhas Current system involving active air–sea interaction is located (Rouault et al. 2002) and indicate that the strongest variance occurs during the austral summer [December–February (DJF)] (Fig. 1d). Meanwhile, another center of the large SST variance to the east of Madagascar is also noticed, in particular during the austral winter [June–August (JJA)] (Fig. 1b) and spring [September–November (SON)] (Fig. 1c),

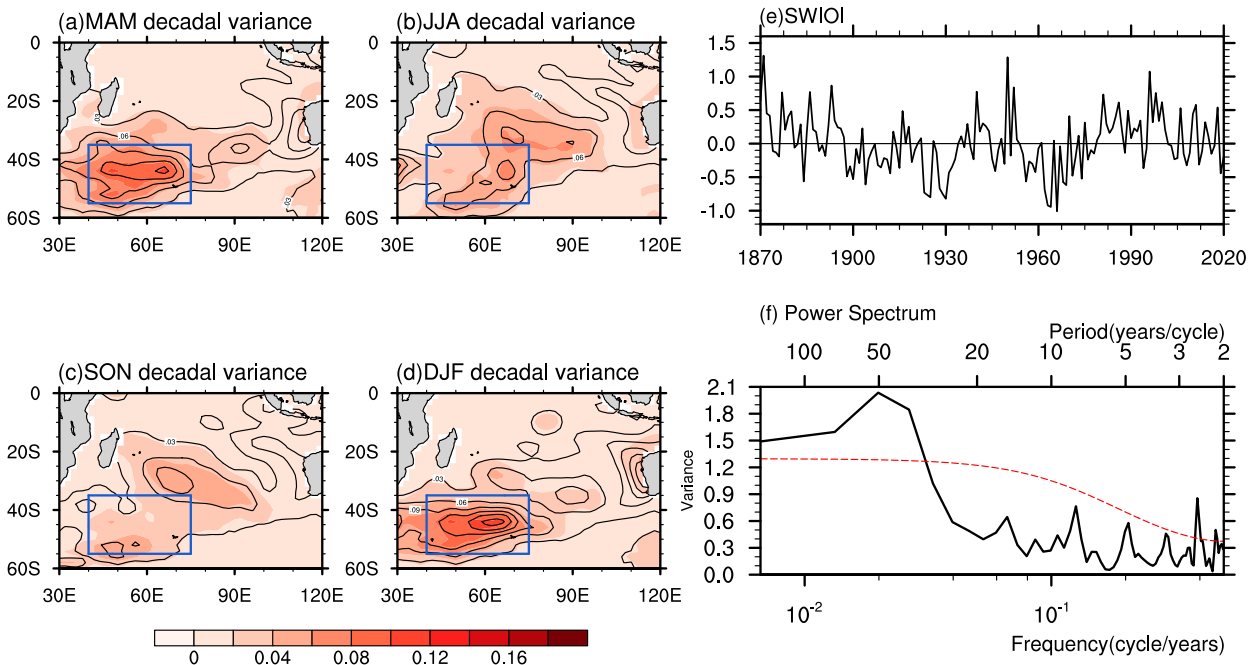


FIG. 1. Spatial distributions of the SST variance for (a) MAM, (b) JJA, (c) SON, and (d) DJF based on observations. The contour represents decadal-filtered component (>8 years) and the shading represents the multidecadal-filtered component (>17 years). The domain in the blue box represents the region of the SWIO. (e) Time series of the SWIOI from 1870 to 2020 in DJF. (f) Power spectrum of the SWIOI from 1870 to 2020 in DJF. The dashed line indicates the 90% confidence level.

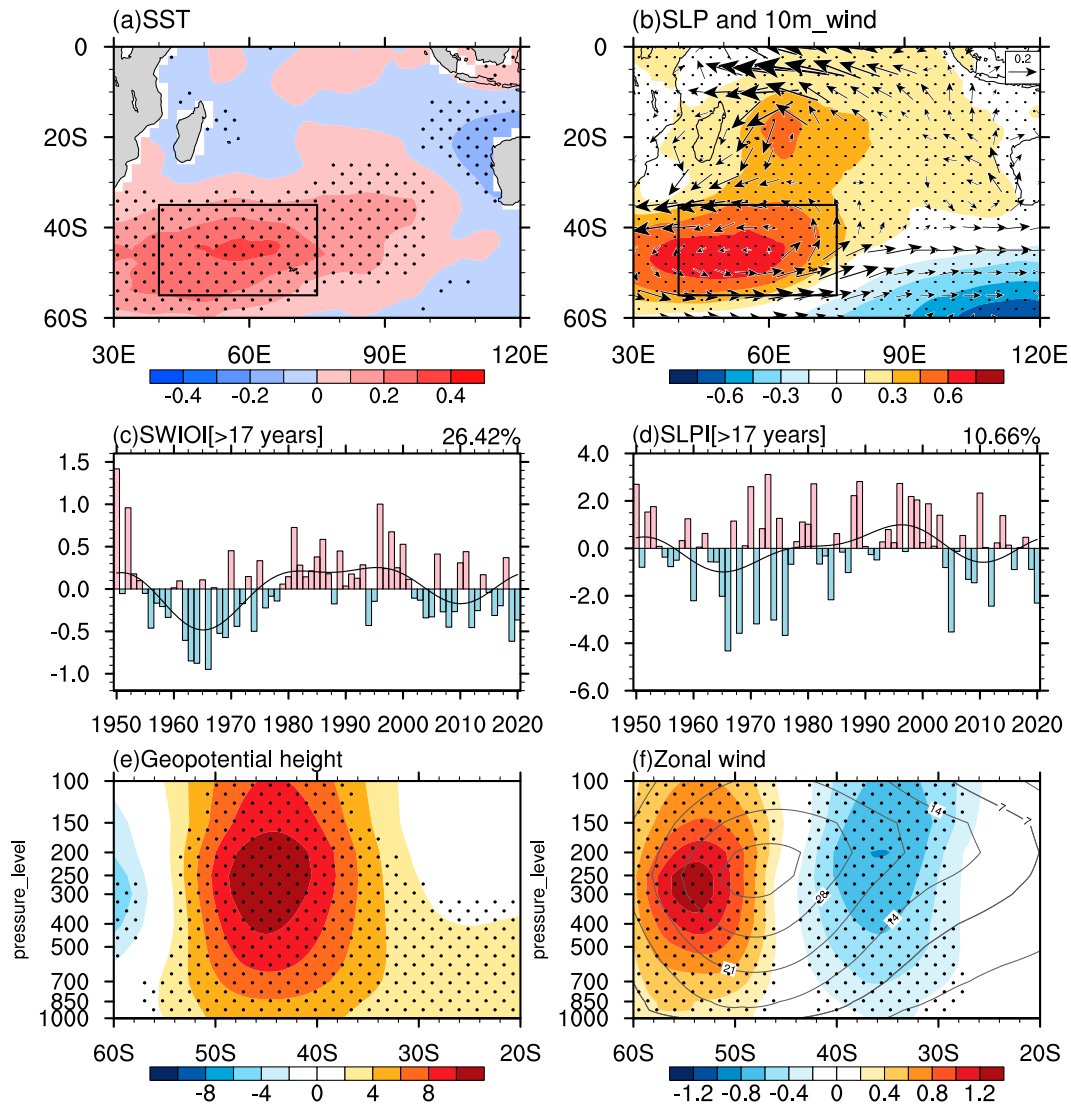


FIG. 2. Regression maps of (a) SST (shaded;  $^{\circ}\text{C}$ ), (b) SLP (shaded; hPa) and 10-m wind (vectors;  $\text{m s}^{-1}$ ) in DJF onto the multidecadal-filtered SWIOI. Time series of (c) SWIOI (bar) and (d) SLPI (bar) and their multidecadal components (black lines) based on observations/reanalysis in DJF from 1950 to 2020. Regression distributions in pressure–latitude cross section of (e) geopotential height (shaded; m) and (f) zonal wind (shaded;  $\text{m s}^{-1}$ ) zonally averaged over  $40^{\circ}$ – $75^{\circ}\text{E}$  in DJF onto the multidecadal-filtered SWIOI. The contours in (f) represent the climatological zonal wind in DJF. The stippling indicates the anomaly exceeding the 95% confidence level, and the domain in the black box represents the SWIO.

which is associated with an anomalous geostrophic current along the western boundary (Li and Su 2021) and significantly weaker than that in the southwestern Indian Ocean. In the present study, we focus on the low-frequency variability in the southwestern Indian Ocean (SWIO;  $55^{\circ}$ – $35^{\circ}\text{S}$ ,  $40^{\circ}$ – $75^{\circ}\text{E}$ ; shown as the box in Fig. 1). The area-averaged SST anomalies within it during DJF are defined as the SWIO index (SWIOI; Fig. 1e), which shows significant interannual variability of 2–3 years and multidecadal variability of about 50 years (Fig. 1f). Although decadal variability of about 10 years can also be observed, it does not pass the significance test, indicating the dominance of the multidecadal time scale in the low-frequency variability of SST in the SWIO (Fig. 1f).

Figure 2 illustrates the characteristics of the air–sea coupling system in the SWIO on the multidecadal time scale based on observations/reanalysis. Positive SST anomalies with a magnitude of  $0.3^{\circ}$ – $0.4^{\circ}\text{C}$  are observed in the SWIO (Fig. 2a), accompanied by high pressure anomalies and anomalous easterly (westerly) wind near  $40^{\circ}\text{S}$  ( $55^{\circ}\text{S}$ ) (Fig. 2b). Besides, negative SST anomalies appear along the coast of western Australia (Fig. 2a), which may be related to Ningaloo Niño (Feng et al. 2013; Ryan et al. 2021). Based on the area-averaged SLP anomalies during DJF in the SWIO region, an SLP index (SLPI) is defined to display the SLP evolution. Notably, the SWIOI and SLPI time evolutions exhibit good

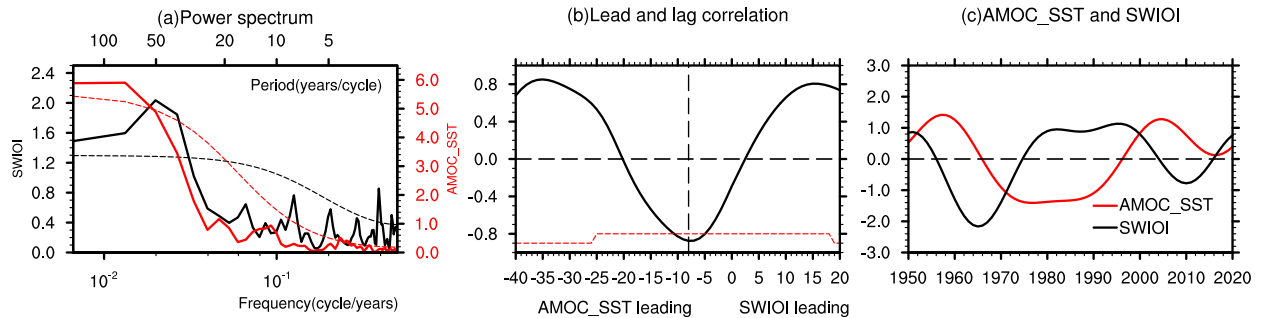


FIG. 3. (a) Power spectrum of SWIOI (black) and AMOC\_SST (red) from 1870 to 2020, (b) lead and lag correlations between AMOC\_SST index and SWIOI on multidecadal time scale, and (c) normalized time series of multidecadal-filtered AMOC\_SST (red) and SWIOI (black) based on observations. The dashed lines in (a) and (b) indicate the 90% confidence level.

consistency on the multidecadal time scale with a high correlation coefficient of 0.92 (Figs. 2c,d). The maximum magnitude of the multidecadal anomalies of SST and SLP can reach  $0.5^{\circ}\text{C}$  (Fig. 2c) and 1 hPa (Fig. 2d), and the multidecadal variability can account for 26.42% (Fig. 2c) and 10.66% (Fig. 2d) of the total variance of SWIOI and SLPI. Furthermore, regressions of geopotential height and zonal wind averaged over  $40^{\circ}$ – $75^{\circ}\text{E}$  at the pressure–latitude cross section clearly present that the anomalous atmospheric geopotential height exhibits high pressure anomalies with the center at 300 hPa (Fig. 2e), known as equivalent barotropic warm/ridge structure (Fang and Yang 2016). The westerly (easterly) wind anomalies prevail from surface to above 100 hPa in the mid-latitude (subtropics), representing the poleward shift of the westerly jet (Fig. 2f). In summary, the multidecadal variability of the SWIO is characterized by a significant equivalent barotropic high (low) pressure anomaly over the warm (cold) SST and a poleward (equatorward) shift of the westerly wind during its positive (negative) phase. In the following section, we will examine the mechanisms including the remote forcings and the local processes that are responsible for the multidecadal variability in the SWIO.

#### 4. Potential modulation of the AMOC on the multidecadal variability of the southern Indian Ocean

##### a. Observation

To explore possible remote influences on the SWIO multidecadal variability, the regression maps of SST leading from 30 to 0 years during the austral summer on the SWIOI are illustrated in Fig. S1 in the online supplemental material. As SST leads by up to 30 years, a significant dipole pattern of SST anomalies appears in the Atlantic Ocean with positive values over the NA and negative ones over the SA, and negative anomalies in the SWIO are relatively weak (Fig. S1a). This dipole pattern of SST anomalies in the Atlantic has been suggested as the result of the anomalous interhemispheric ocean heat transport associated with AMOC variation (Latif et al. 2006; Sun et al. 2013, 2018; Orihuela-Pinto et al. 2022). Along with the fading of the Atlantic SST anomalies, significantly negative SST anomalies gradually develop in the SWIO (Figs. S1b,c). Subsequently, when the Atlantic dipolar

SST anomalies reverse sign, with negative (positive) anomalies in the NA (SA), the warm SST anomalies occur and amplify in the SWIO (Figs. S1d–f). Further analysis is performed on the AMOC\_SST and SWIOI (Fig. 3), and their power spectrums indicate a predominant variance at the roughly common period between 50 and 100 years (Fig. 3a). Meanwhile, AMOC\_SST and SWIOI time series present significantly negative correlation ( $-0.88$ ) when the AMOC leads by 8 years (Figs. 3b,c). These results manifest that the multidecadal variability of the SWIO is likely to be associated with the preceding AMOC variation.

Figure 4 presents the multidecadal SST and SLP regression anomalies when they lag the AMOC\_SST from 0 to 30 years. At 0-yr lag, a dipole pattern of interhemispheric SST anomalies is located in the Atlantic Ocean, with warm (cold) anomalies in the midlatitude NA (SA) (Fig. 4a). Meanwhile, two high pressure anomaly centers appear to the southwest of Africa and Australia and a low pressure anomaly center occurs at high latitudes (Fig. 4a). With the decline of the Atlantic SST anomalies, negative SST anomalies and an anomalous low pressure gradually establish in the SWIO several years later to form the cold/trough structure (Figs. 4b,c). At 18-yr lag, the AMOC\_SST transforms into its negative phase (Fig. 4d) and the associated anomalies of SST and SLP are a mirror image to its positive phase (Fig. 4a). In the subsequent years, the warm SST forms and the low pressure turns into a weak high pressure in the SWIO (Figs. 4e,f). For more clear SST evolutions associated with the AMOC\_SST, the time–longitude section of mixed layer heat content (OHC) anomalies averaged at  $55^{\circ}$ – $40^{\circ}\text{S}$  is illustrated (Fig. S2). The latitude band here is slightly narrower than the  $55^{\circ}$ – $35^{\circ}\text{S}$  in which the SWIO is defined to avoid the influence of the westward Agulhas Current on the coast of southern Africa. Significant eastward propagation is observed from the eastern SA ( $15^{\circ}\text{W}$ – $0^{\circ}$ ) to the SWIO ( $40^{\circ}$ – $75^{\circ}\text{E}$ ) with a speed of  $0.02\text{ m s}^{-1}$  estimated by the distance between the center of OHC anomalies in the SA ( $15^{\circ}\text{W}$ ) and the SWIO ( $60^{\circ}\text{E}$ ) along the  $50^{\circ}\text{S}$  dividing the time when the correlation between the AMOC index and SWIOI is the maximum. It is found that the speed of the eastward propagation is comparatively slower than the speed of  $0.09\text{ m s}^{-1}$  of the upper ocean mean zonal current at  $15^{\circ}$ – $60^{\circ}\text{E}$ . These results suggest that the multidecadal SST variations in the SWIO may be

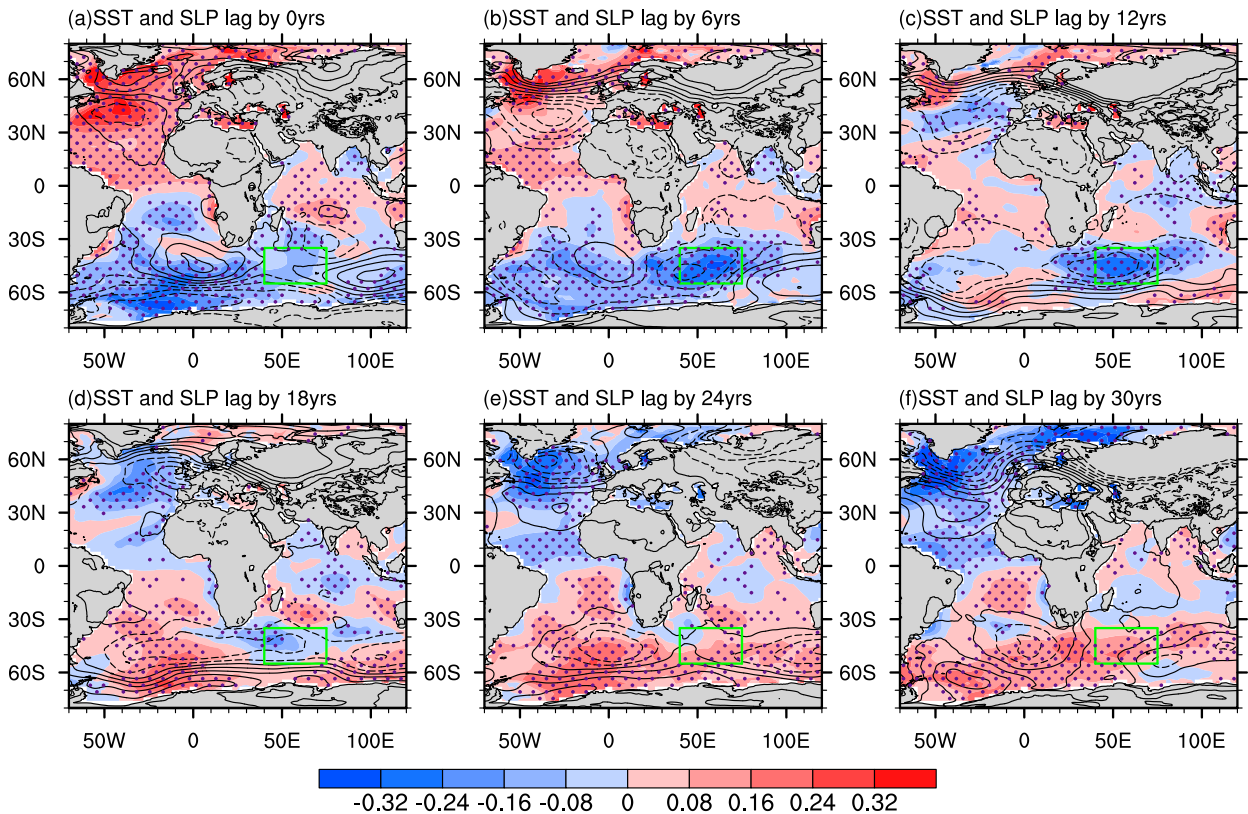


FIG. 4. Regression maps of SST (shaded;  $^{\circ}\text{C}$ ) and SLP (contours; hPa) at different lags for (a) 0, (b) 6, (c) 12, (d) 18, (e) 24, and (f) 30 years in DJF onto the multidecadal-filtered AMOC\_SST index based on observations/reanalysis. The stippling indicates the anomalies exceeding the 95% confidence level. The domain in the green box represents the SWIO.

influenced by the AMOC-related OHC (SST) propagating from the SA and then amplified by the local air–sea positive feedback in the SWIO. Due to the limitation of the short observation, CMIP6 model simulations will be utilized to investigate the abovementioned mechanism in the following section.

#### b. CMIP6 model simulations

In model simulations, the AMOC\_SF is used to represent the AMOC variation. According to previous studies, the AMOC variation is closely related to the SST variation in the midlatitude Atlantic Ocean (Latif et al. 2006; Dima and Lohmann 2010). As is expected, the AMOC\_SF and AMOC\_SST are positively correlated although the correlation reaches maximum at different lags among different models (Table 1). Both AMOC\_SF and AMOC\_SST show a similar multidecadal period (figure not shown) in most of the models, except CanESM5 which will not be considered later. To investigate the impact of the AMOC on the SWIO multidecadal SST variability, the power spectrum analysis was performed to select the models, in which the AMOC\_SF has a similar multidecadal period as the SWIO. There are five models (FGOALS-g3, GFDL-CM4, HadGEM3-GC3.1-LL, MIROC6, and MRI-ESM2-0) that satisfy the requirement (Fig. 5). The SWIO and AMOC\_SF have the shortest multidecadal period of about 25 years in FGOALS-g3 (Fig. 5e) and the longest period around 100 years in GFDL-CM4 and MIROC6 (Figs. 5f,i). In terms of

HadGEM3-GC3.1-LL and MRI-ESM2-0, the common period of the AMOC\_SF and SWIO is approximately 50 years (Figs. 5h,j). Although the AMOC\_SF shows a similar multidecadal period as the SWIO in these five models, a significantly negative relationship between AMOC\_SF and SWIO is only obtained in GFDL-CM4 and HadGEM3-GC3.1-LL (Table S1). Consequently, GFDL-CM4 and HadGEM3-GC3.1-LL will be used to investigate the impact of the AMOC on the multidecadal variability of SWIO. For the GFDL-CM4 model, although the AMOC\_SF presents significant period of about 50 and 100 years, there is no peak of the variance around 50 years for the SWIO (Fig. 5f), so the period of the AMOC shorter than 60 years will not be considered in this model. The period shorter than 30 years will also be excluded to focus on the period around 50 years in HadGEM3-GC3.1-LL. The possible reasons for the poor relationship between AMOC\_SF and SWIO in the other three models will be discussed later.

The magnitude of the multidecadal SST anomalies in the SWIO can reach about  $0.3^{\circ}\text{C}$  and account for 11.26% and 23.92% of the total variance of SST variation in HadGEM3-GC3.1-LL and GFDL-CM4 (figure not shown). As shown in Fig. 6a, the AMOC\_SF and SWIO have a maximum correlation coefficient of  $-0.33$  when the AMOC leads SWIO by 13 years in HadGEM3-GC3.1-LL. It is worth noting that the period of AMOC shows a relatively long period of about 100 years after 200 years (Fig. 6b), which can explain its

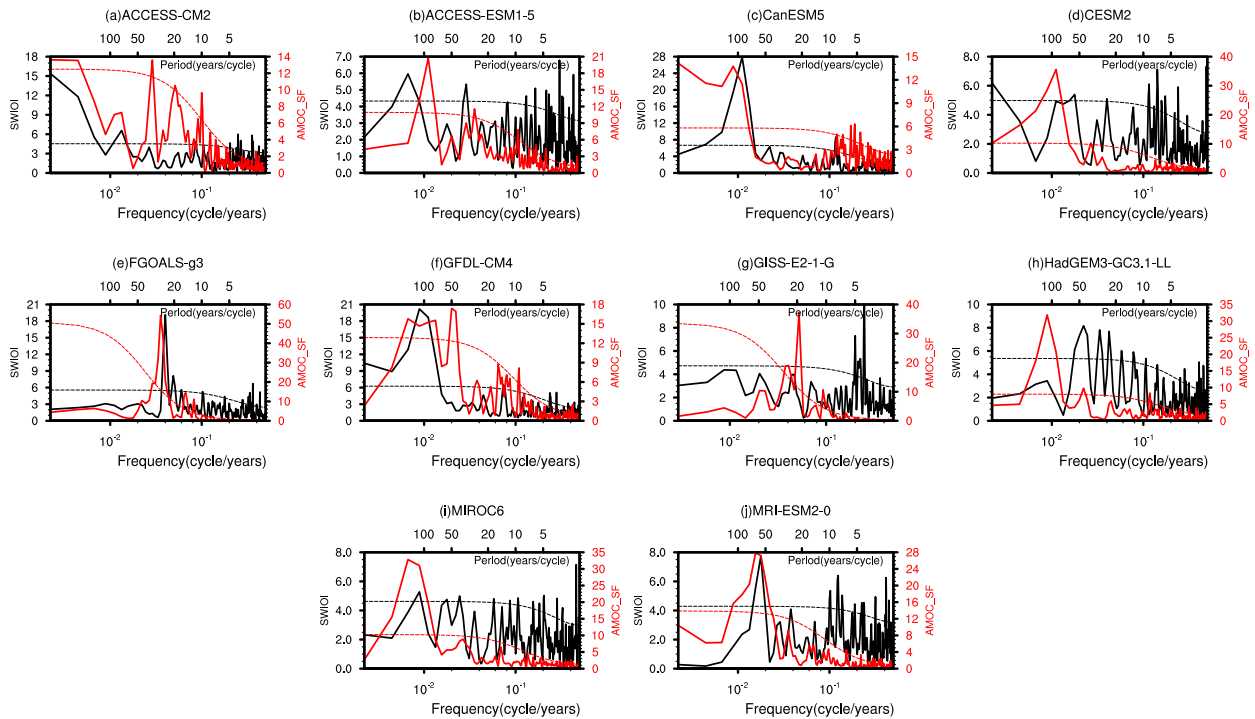


FIG. 5. Power spectra of the SWIOI (black) and AMOC\_SF (red) in the CMIP6 model preindustrial simulations.

pronounced variance at 100 years in the power spectrum (Fig. 5h). Despite this unstable period of the AMOC in the 450 years simulation, the phase of the SWIOI is still likely to be the opposite of AMOC after 200 years (Fig. 6b). In terms of GFDL-CM4, a strong negative correlation reaching  $-0.64$  is found at the AMOC leading by 10 years (Fig. 6c) and these two indices also exhibit clearly opposite evolutions and a long period of about 100 years (Fig. 6d).

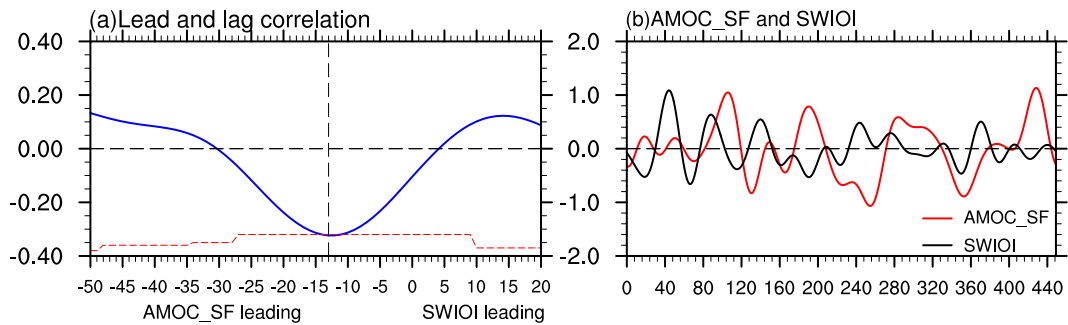
The regression maps of SST and SLP onto the AMOC\_SF on the multidecadal time scale for HadGEM3-GC3.1-LL and GFDL-CM4 are taken to investigate the possible mechanism of the AMOC linking the SWIO multidecadal variability (Fig. 7). As for HadGEM3-GC3.1-LL, associated with the positive phase of AMOC are positive SST anomalies in the NA pole and negative ones in the SA pole, accompanied by high pressure anomalies to the south of Africa and southwest of Australia at 0-yr lag (Fig. 7a), resembling the pattern in observations (Fig. 4a). At 15-yr lag, the negative SST anomalies spread to the SWIO and a low pressure anomaly forms over these cold anomalies (Fig. 7b). Whereafter, with the AMOC shifting to a negative phase, the SST anomalies gradually reverse in the midlatitudes of the Atlantic Ocean (Fig. 7c). Correspondingly, under the effect of the east-

ward propagation of the warm SST anomalies from the SA, positive SST anomalies and anomalous high pressure develop in the SWIO, and the significantly negative SST anomalies with the low pressure anomaly propagate downstream to the southeastern Indian Ocean and then decay (Figs. 7c,d). The distributions of the SST and SLP in GFDL-CM4 bear some similarities to those features in HadGEM3-GC3.1-LL although the time scale of multidecadal variability is longer. The out-phase SST anomalies start to appear in the NA pole and SA pole at 0-yr lag (40-yr lag) (Figs. 7e,g), representing the positive (negative) phase of the AMOC. Similarly, strong negative (positive) SST anomalies with a low (high) pressure occur in the SWIO after decades (Figs. 7f,h). Like observations, the SST anomalies in the SWIO also seem to be affected by the eastward propagating SST anomalies related to the AMOC from the SA and then amplified by the local air-sea positive feedback in the SWIO in models.

To examine the mechanisms responsible for relationships on AMOC–SWIO SST variability connection, the equation for the temperature tendency anomaly in the mixed layer is utilized, which is estimated as below (Stevenson and Niiler 1983; Jin et al. 2006):

$$\frac{\partial T'}{\partial t} = \frac{Q'}{\rho C_p H} + \underbrace{\left( -u' \frac{\partial \bar{T}}{\partial x} - \bar{u} \frac{\partial T'}{\partial x} - u' \frac{\partial T'}{\partial x} \right)}_{ZA} + \underbrace{\left( -v' \frac{\partial \bar{T}}{\partial y} - \bar{v} \frac{\partial T'}{\partial y} - v' \frac{\partial T'}{\partial y} \right)}_{MA} + \underbrace{\left( -w'_e \frac{\partial \bar{T}}{\partial z} - \bar{w}_e \frac{\partial T'}{\partial z} - w'_e \frac{\partial T'}{\partial z} \right)}_{VA}, \quad (2)$$

## HadGEM3-GC3.1-LL



## GFDL-CM4

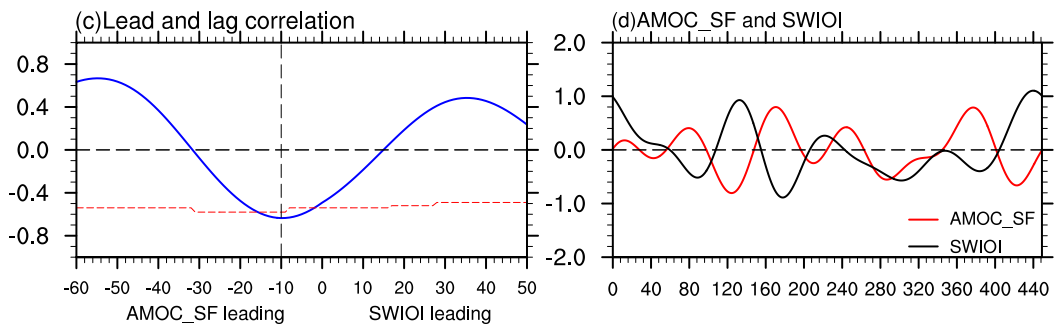


FIG. 6. (a) Lead and lag correlations between the multidecadal-filtered AMOC\_SF and SWIOI, and (b) normalized time series of the multidecadal-filtered AMOC\_SF (red) and SWIOI (black) in HadGEM3-GC3.1-LL. (c),(d) As in (a) and (b), but for GFDL-CM4. Dashed lines in (a) and (c) indicate the 90% confidence level.

where  $T$ ,  $u$ ,  $v$ , and  $w_e$  denote temperature, zonal and meridional components of ocean currents in the mixed layer, and the entrainment velocity. The temperature vertical gradient is calculated by the temperature difference between the upper and the bottom of mixed layer. The overbar and prime stand for mean states and deviation from the climatology. The terms on the right side of the equation represent the net surface heat flux and radiation ( $Q_{net}$ ), zonal and meridional temperature advection, and entrainment process (ZA, MA, and VA). Each advection term includes three components, which are the advectations of mean temperature gradients by anomalous currents (ZA1, MA1, and VAI), advectations of anomalous temperature gradients by mean currents (ZA2, MA2, and VA2), and the nonlinear terms (ZA3, MA3, and VA3). The terms  $\rho$ ,  $C_p$ , and  $H$  are the seawater density, specific heat of seawater, and the climatological ocean mixed layer thickness. Furthermore,  $Q$  can be decomposed as follows:

$$Q = LH + SH + SW + LW, \quad (3)$$

where LH, SH, SW, and LW denote latent heat flux, sensible heat flux, shortwave radiation, and longwave radiation at the surface, respectively, with positive values representing ocean gaining heat.

Although many studies have demonstrated the impact of the AMOC on the SA SST through changing the oceanic meridional heat transport (Vellinga and Wood 2002; Latif et al.

2004, 2006; Sun et al. 2018), it is necessary to verify this mechanism in HadGEM3-GC3.1-LL and GFDL-CM4 before using them to investigate the impact of AMOC on the SWIO SST. As shown in Figs. S3 and S4, when the SA SST is cold (Figs. S3a and S4a), significantly negative MA1 anomalies appear in the SA and along the east coast of South America (Figs. S3c and S4c), representing the weakening of the Brazil Current that is closely related to the AMOC variation (Schmid and Majumder 2018; Chidichimo et al. 2023). Due to the possible influence of the wind stress on the surface ocean current, the meridional advection anomalies caused by the anomalous current associated with the AMOC in the top 500 m (MA500) over the SA were also examined (Fig. 15). The strong negative MA500 anomalies between 60° and 40°S are evident in these two models, indicating its cooling effect on the SA (Figs. 15f,h). Meanwhile,  $Q_{net}$  and ZA2 display positive anomalies, favoring the damping of the cold water in the SA (Figs. S3b,d and S4b,d), and the other processes show minor effects (Figs. S3e and S4e). These results indicate that the multidecadal temperature anomalies in the SA are predominantly induced by the meridional advection of mean meridional temperature gradient by anomalous meridional current related to the AMOC.

To investigate the influence of the AMOC on the multidecadal SWIO SST, the regression maps of ZA2,  $Q_{net}$ , and MA1, which have large magnitudes, onto the multidecadal-filtered AMOC\_SF index, are presented in Figs. 8 and 9. For

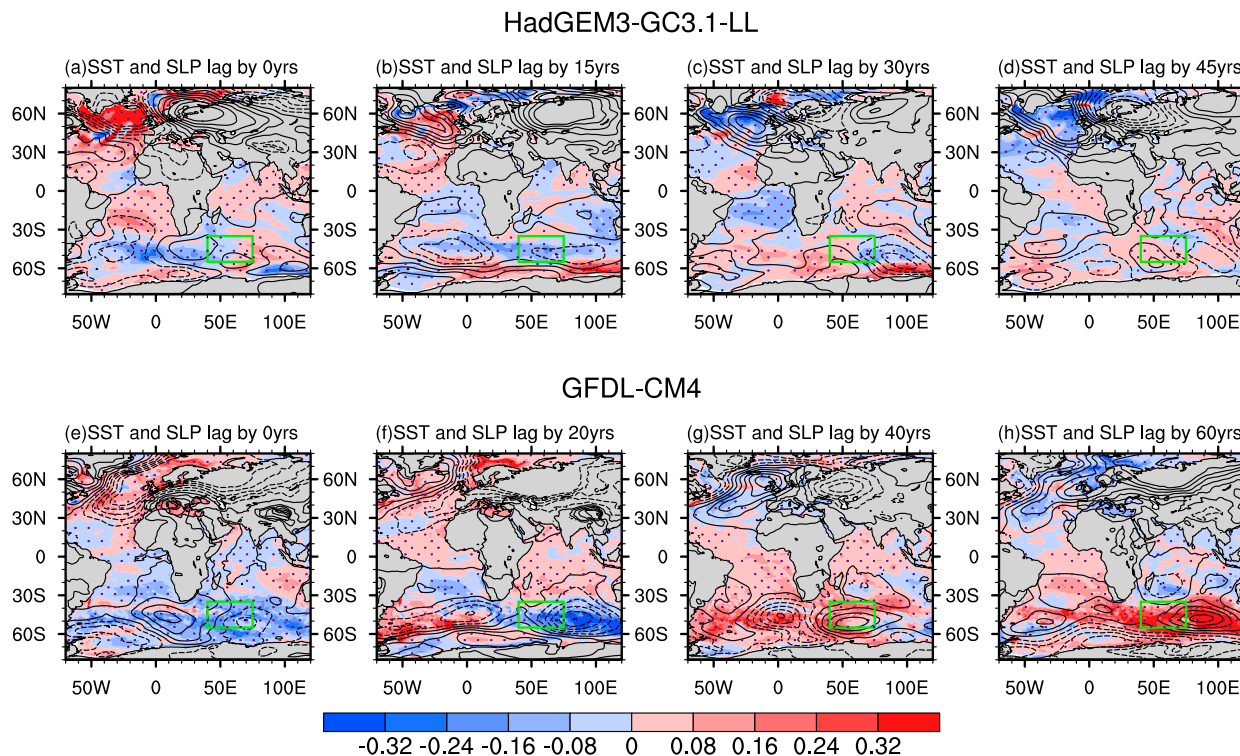


FIG. 7. Regression maps of SST (shaded;  $^{\circ}\text{C}$ ) and SLP (contours; hPa) at different lags for (a) 0, (b) 15, (c) 30, and (d) 45 years in DJF onto the multidecadal-filtered AMOC\_SF in HadGEM3-GC3.1-LL. (e)–(h) As in (a)–(d), but for SST and SLP lagging from 0 to 60 years in GFDL-CM4. The stippling indicates the anomalies exceeding the 95% confidence level, and the domain in the green box represents the SWIO.

HadGEM3-GC3.1-LL, with the negative (positive) SST anomalies in the SA (Figs. 7a,c), there are remarkably negative (positive) ZA2 anomalies in the SWIO at 0-yr lag (30-yr lag), conducive to the cooling (warming) of the SWIO (Figs. 8a,c). These results suggest that the SA SST may affect SWIO SST through the advection of anomalous temperature by the mean zonal current. Once positive (negative) SST anomalies spread from the SA to the SWIO, they act to create an overlying anticyclone (cyclone) at the sea level and in the troposphere through transient eddy feedback, which will be examined in section 5. These changes in circulation provide local positive feedback on the initial SST anomalies through changing  $Q_{\text{net}}$  and MA1. This positive feedback can be observed since the 15-yr lag when the low pressure anomaly establishes in HadGEM3-GC3.1-LL (Fig. 7b). At the 15-yr lag, the anomalous westerlies in the northern flank of the low pressure anomalies tend to strengthen the local westerlies, which lead to enhanced upward turbulent heat fluxes and negative  $Q_{\text{net}}$  anomalies (Figs. 7b and 8f). At the 30-yr lag, the negative  $Q_{\text{net}}$  anomalies are gradually replaced by the positive ones due to anomalous easterlies on the north side of the developing high pressure anomaly (Figs. 7c and 8g). Besides, the local air–sea interaction also modulates the MA1 to enhance the SST anomalies. Due to the anomalous southerlies in the west flank of the low pressure, the anomalous equatorward current transports the colder water to the SWIO region from

high latitudes, leading to the negative MA1 anomalies at 15-yr lag (Figs. 7b and 8j). At 30-yr lag, the negative SST anomaly and the low pressure anomaly propagate downstream. Although the negative MA1 anomalies caused by the anomalous southerlies in the west flank of the low pressure anomaly still tend to maintain the cold water, the positive SST anomalies are already generated due to the warm water propagating from the SA (Figs. 7c and 8k). Subsequently, with the development of the anomalous high pressure and the anomalous northerlies in its west flank (Fig. 7d), the positive MA1 anomalies appear in the SWIO induced by the poleward current anomalies at 45-yr lag (Fig. 8l). It is worth noting that there are also obvious negative  $Q_{\text{net}}$  anomalies in the SWIO at the 0-yr lag, which may result from the enhanced wind speed caused by the anomalous westerlies to the south of the anticyclonic circulation at  $0^{\circ}$ – $70^{\circ}\text{E}$  (Figs. 7a and 8e). Similar high pressure anomalies spanning midlatitudes of the southern Indian Ocean can also be observed in observations (Fig. 4a), which may be related to the Atlantic multidecadal oscillation (AMO) via atmospheric teleconnection (Li et al. 2014; Simpkins et al. 2014; Zhu et al. 2021). Although the AMO can impact the SWIO SST, this simultaneous effect is not consistent with the highest correlation between the AMOC and the SWIO SST when AMOC leads by a decade, indicating a more important role of the eastward propagating temperature anomalies from the SA.

## HadGEM3-GC3.1-LL (SWIO)

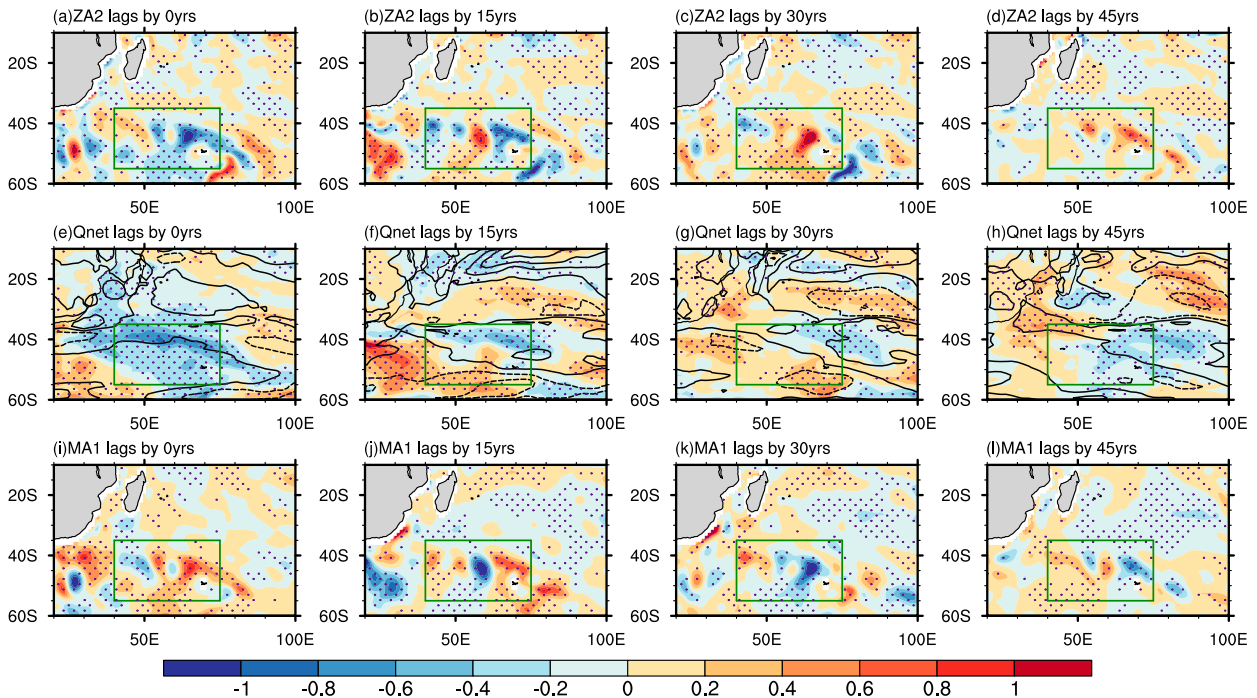


FIG. 8. Regression maps of (a)–(d) ZA2 (shaded;  $^{\circ}\text{C yr}^{-1}$ ), (e)–(h)  $Q_{\text{net}}$  (shaded;  $^{\circ}\text{C yr}^{-1}$ ), 10-m wind speed (contours;  $\text{m s}^{-1}$ ), and (i)–(l) MA1 (shaded;  $^{\circ}\text{C yr}^{-1}$ ) at different lags from 0 to 45 years in DJF onto the multidecadal filtered AMOC\_SF in HadGEM3-GC3.1-LL. The stippling indicates the anomalies exceeding the 95% confidence level, and the domain in the green box represents the SWIO.

As for the GFDL-CM4 model, when the AMOC is in the positive phase, there are negative SST anomalies in the SA and negative ZA2 anomalies in the south of SWIO (Figs. 7e and 9a). With AMOC gradually turning into its negative phase, the warm SST occurs in the SA (Figs. 7f,g) and positive ZA2 anomalies appear in the SWIO at 15- and 30-yr lags (Figs. 9b,c). These results also indicate the possible effect of the SA SST on the SWIO via mean zonal current in GFDL-CM4. Meanwhile, the local air–sea positive feedback in the SWIO is also clear. Different from HadGEM3-GC3.1-LL, the low pressure anomaly already exists in the SWIO at 0-yr lag, which may be induced by the underneath weak negative SST anomalies (Fig. 7e). The anomalous westerlies (easterlies) in the north flank of the low (high) pressure anomaly in the SWIO increase (decrease) the local westerlies (Figs. 7e–h), resulting in significantly negative (positive)  $Q_{\text{net}}$  anomalies (Figs. 9e–h). Additionally, the anomalous equatorward (poleward) currents driven by anomalous southerlies (northerlies) in the west flank of the low (high) pressure cause the negative (positive) MA1 in the SWIO (Figs. 9i–l), also acting to amplify the negative (positive) SST anomalies of the SWIO.

To quantify the relative contribution of each process mentioned above to the multidecadal variability of the SWIO SST, the mixed layer heat budget over the SWIO is analyzed. The area-averaged mixed layer temperature anomalies, SLP anomalies, and each term of Eqs. (2) and (3) in the SWIO in a quarter period are constructed by regressing them onto the multidecadal-filtered SWIOI as the SWIOI lags from 0 years

to decades. For HadGEM3-GC3.1-11, a quarter period of the mixed layer temperature in the SWIO is about 13 years, which is consistent with the significant period of about 50 years of the SWIOI (Fig. 5h). The enhancement of the pressure anomaly lags the increasing mixed layer temperature, suggesting that the pressure anomaly is likely to be induced by the underlying SST anomaly, which will be discussed in section 5. During the development of the positive temperature anomaly, the ZA2 anomaly remains positive, representing the influence of the SA temperature anomalies on the SWIO via the mean zonal current advection (Fig. 10c). As discussed above, once the temperature anomalies reach the SWIO, the local air–sea positive feedback is excited to amplify the SWIO temperature anomalies via the  $Q_{\text{net}}$  and MA1. The initial negative MA1 anomalies may be induced by the anomalous southerlies between a weak high pressure anomaly over the SWIO and a weak low pressure to its east (figure not shown). However, with the increase in the SLP over the SWIO, the positive anomalies of  $Q_{\text{net}}$  and MA1 gradually enhance (Figs. 10b,c), which reinforce the positive SST anomalies of the SWIO. The  $Q_{\text{net}}$ , in which the LH is slightly larger than the other components, shows a magnitude comparable to the ZA2 and stronger than the MA1 (Figs. 10c,d).

For the GFDL-CM4 model, the mixed layer temperature presents a longer quarter period of about 30 years (Fig. 11a). Similarly, with the increase in the mixed layer temperature, the SLP develops from a negative anomaly to a positive anomaly (Fig. 11a). The positive anomaly of ZA2 contributes

## GFDL-CM4 (SWIO)

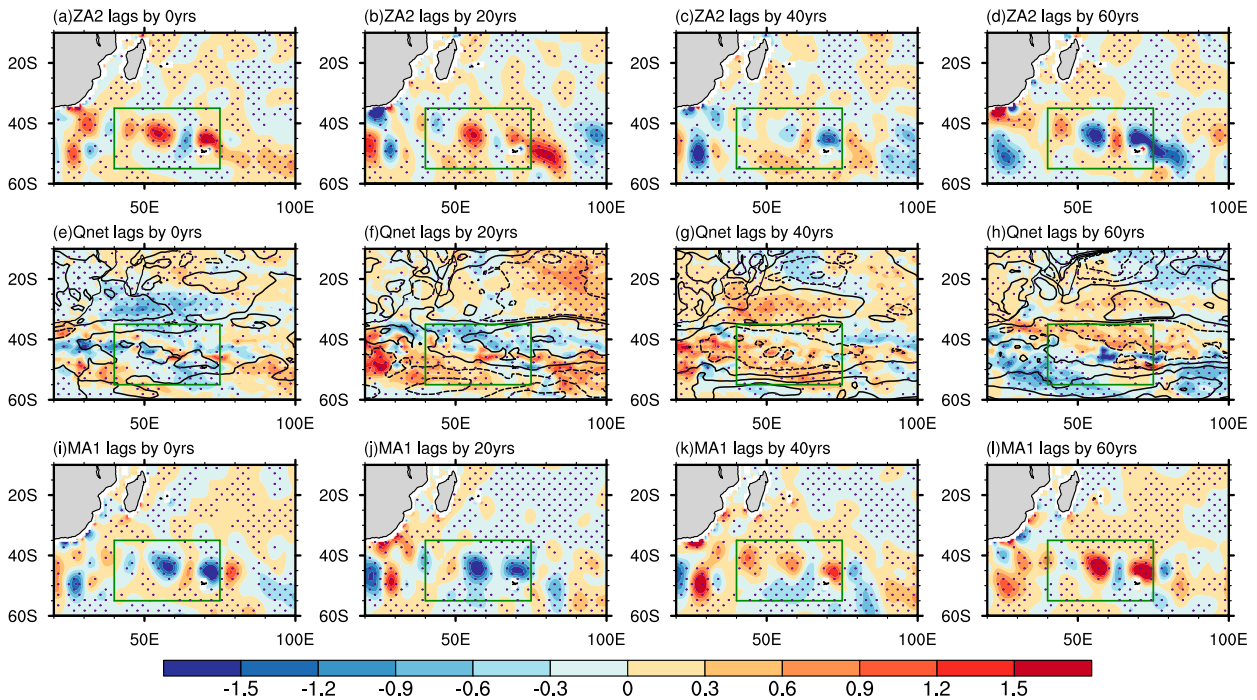


FIG. 9. As in Fig. 8, but for the regressed (a)–(d) ZA2 (shaded;  $^{\circ}\text{C yr}^{-1}$ ), (e)–(h)  $Q_{\text{net}}$  (shaded;  $^{\circ}\text{C yr}^{-1}$ ), 10-m wind speed (contours;  $\text{m s}^{-1}$ ), and (i)–(l) MA1 (shaded;  $^{\circ}\text{C yr}^{-1}$ ) at different lags from 0 to 60 years in GFDL-CM4.

to the increased temperature in the first 6 years (Fig. 11c), while ZA2 is relatively weaker than that in HadGEM3-GC3.1-11. After ZA2 shifts to the negative anomaly, MA1 and  $Q_{\text{net}}$  associated with the local air–sea positive feedback tend to sustain the multidecadal SWIO SST anomalies (Figs. 11b,c). Different from HadGEM3-GC3.1-11, the magnitude of  $Q_{\text{net}}$  is significantly weaker than MA1 and seems attributed to weak changes in SH and SW (Fig. 11d). It should be noted that MA2 also presents a significantly positive anomaly in GFDL-CM4 (Fig. 11c), whereas it plays a damping effect in HadGEM3-GC3.1-LL (Fig. 10c). In GFDL-CM4, during the development of the warm water in the SWIO, the strongest warming is not in the center of SWIO, but along the southwest side of the SWIO where the climatological meridional currents are northward (Figs. S5a–c), which cause the positive MA2 anomalies in the SWIO (Figs. S5e–g). This warmer mixed layer temperature along the southwest side of the SWIO is probably associated with stronger positive ZA2 anomalies in the south part of the SWIO (Figs. S5i,j), due to the blocking of weak cool water to the south of Africa (Figs. S5a,b). That is, although the area-averaged ZA2 is relatively weak, the spatial pattern demonstrates its effect on modulating the mixed layer temperature along the southern part of the SWIO, which will further influence the SWIO by MA2. In contrast, the strongest warming is located in the center of the SWIO (Figs. S6a–e) and the positive ZA2 anomalies occur in most regions of the SWIO (Figs. S6i–k), and thus there are no positive MA2 anomalies in HadGEM3-GC3.1-LL (Figs. S6e–h). The roles of ZA2, MA1, MA2, and  $Q_{\text{net}}$  are also examined using

observations/reanalysis (Fig. S7), and their features are similar to those in HadGEM3-GC3.1-LL.

According to the above investigation, the zonal mean current plays a role in the eastward propagation of temperature anomalies in the mixed layer from the SA to the SWIO. But as shown in Fig. S2, the speed of the eastward propagation of the OHC anomalies is significantly slower than the mean zonal current. Therefore, a further examination is illustrated by the time–longitude sections of the anomalies of the ocean heat content (OHC) in the top 500 m and sea surface height (SSH) averaged over  $55^{\circ}$ – $40^{\circ}\text{S}$  in models (Fig. 12). Note that the approximate speeds of this eastward propagation from SA to SWIO, which are  $0.012 \text{ m s}^{-1}$  (HadGEM3-GC3.1-LL) and  $0.016 \text{ m s}^{-1}$  (GFDL-CM4), are significantly slower than the average speed of  $0.07 \text{ m s}^{-1}$  for the eastward mean zonal currents in the top 500 m. As indicated by Morioka et al. (2017), the eastward propagation of the SST anomalies from SA to SWIO may be attributed to the quasi-stationary Rossby wave, which is the superposition of the first baroclinic Rossby wave and the background eastward current (Hughes 1996). In the South Atlantic and south Indian Ocean between  $55^{\circ}$  and  $40^{\circ}\text{S}$ , the typical speed of the westward first baroclinic wave ranges from  $0.03$  to  $0.05 \text{ m s}^{-1}$  (Chelton and Schlax 1996; Cipollini et al. 2001). The velocity of the eastward propagating OHC anomalies roughly matches that of the first baroclinic Rossby wave superimposed on the background eastward current. In Morioka et al. (2015a, 2017), the eastward propagation speed is estimated at  $0.015$ – $0.03 \text{ m s}^{-1}$ , also significantly slower than the zonal mean current speed of

## HadGEM3-GC3.1-LL (SWIO)

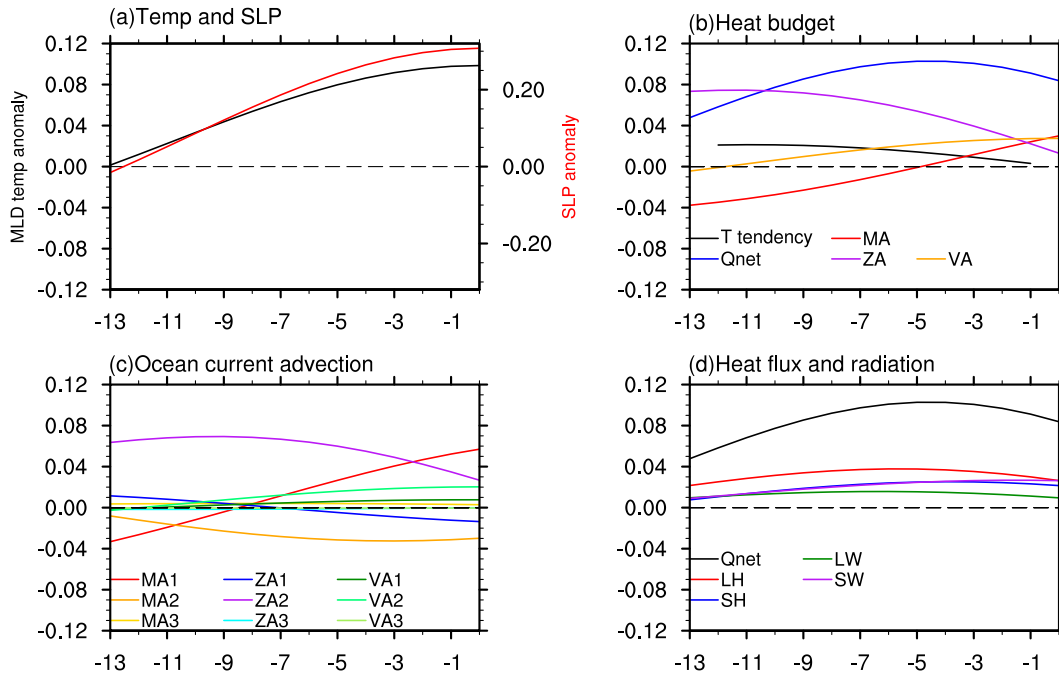


FIG. 10. Time series of the anomalies of (a) mixed layer temperature ( $^{\circ}\text{C}$ ) and SLP (hPa), (b) mixed layer temperature tendency, MA, ZA, VA, and  $Q_{\text{net}}$ , (c) each component of the oceanic current advection, and (d)  $Q_{\text{net}}$  and its components in HadGEM3-GC3.1-LL. These anomalies are obtained by regressing onto the multidecadal-filtered SWIO as the SWIO lags from 13 to 0 years and then averaged over the SWIO. The units of the temperature tendency and each component on the right side of Eqs. (2) and (3) are  $^{\circ}\text{C yr}^{-1}$ .

$0.1 \text{ m s}^{-1}$ . Moreover, the SSH anomalies show a fairly similar eastward propagation as OHC anomalies, suggesting a possible role of the oceanic Rossby wave. Therefore, aside from the contribution from the mean zonal currents, the oceanic Rossby wave driven by the Antarctic Circumpolar Current (ACC) probably plays a more important role to propagate the temperature anomalies from the SA to the SWIO (Morioka et al. 2017).

In conclusion, the mean zonal current plays a role in propagating the AMOC-related SST anomalies from the SA to SWIO, but considering the slow speed of the eastward propagation of the OHC and the coincident eastward propagation of the SSH anomalies from SA to SWIO, the role of the oceanic Rossby wave driven by the ACC may play a more crucial role in linking the SA with SWIO. Once the SST anomalies reach the SWIO, it will induce the local atmospheric circulation anomalies that have positive feedback on the SST anomalies by modulating MA1 and  $Q_{\text{net}}$ . In the following section, the mechanism by which the SST anomalies excite the atmospheric circulation anomaly will be examined in both observations and models.

### 5. The local air–sea feedback in the southern Indian Ocean

Previous studies have demonstrated the existence of an oceanic front in the midlatitude SIO, acting to maintain the

mean surface air temperature (SAT) and thereby anchor the associated storm track and modulate westerly jet via the oceanic baroclinic adjustment (Nakamura et al. 2004, 2008; Sampe et al. 2010; Ogawa et al. 2016), with the most apparent coupling in the austral summer (L. Zhang et al. 2018, 2020). The variation of SST in the oceanic front region can significantly influence atmospheric circulation via modulating synoptic transient eddy activities (Deser et al. 2007; Nakamura 2012; Morioka et al. 2015b; Fang and Yang 2016; Zhang et al. 2021). To investigate this transient eddy-mediated process in midlatitude SIO on the multidecadal time scale, the influence of SST on the storm track activities and further the eddy forcing on the large-scale atmospheric circulation will be investigated in this section.

For describing the storm track activity associated with synoptic eddies, a poleward heat flux ( $\overline{v'T'}$ ) at 850 hPa and meridional flux of westerly momentum ( $\overline{v'u'}$ ) at 250 hPa on synoptic time scale are analyzed (Nakamura et al. 2004; Nakamura 2012; Morioka et al. 2015b). Here,  $u$ ,  $v$ , and  $T$  denote zonal wind, meridional wind, and air temperature, respectively. The overbar and prime represent the seasonal mean and transient perturbation, respectively. We first removed the monthly climatology and long-term trend from the daily data to obtain the anomalies of each variance ( $v'$ ,  $u'$ ,  $T'$ ) from October to March and then extracted the period shorter than 8 days. Finally,  $\overline{v'T'}$  and  $\overline{u'v'}$  are computed and averaged in DJF. The atmospheric baroclinicity is diagnosed by the Eady

GFDL-CM4 (SWIO)

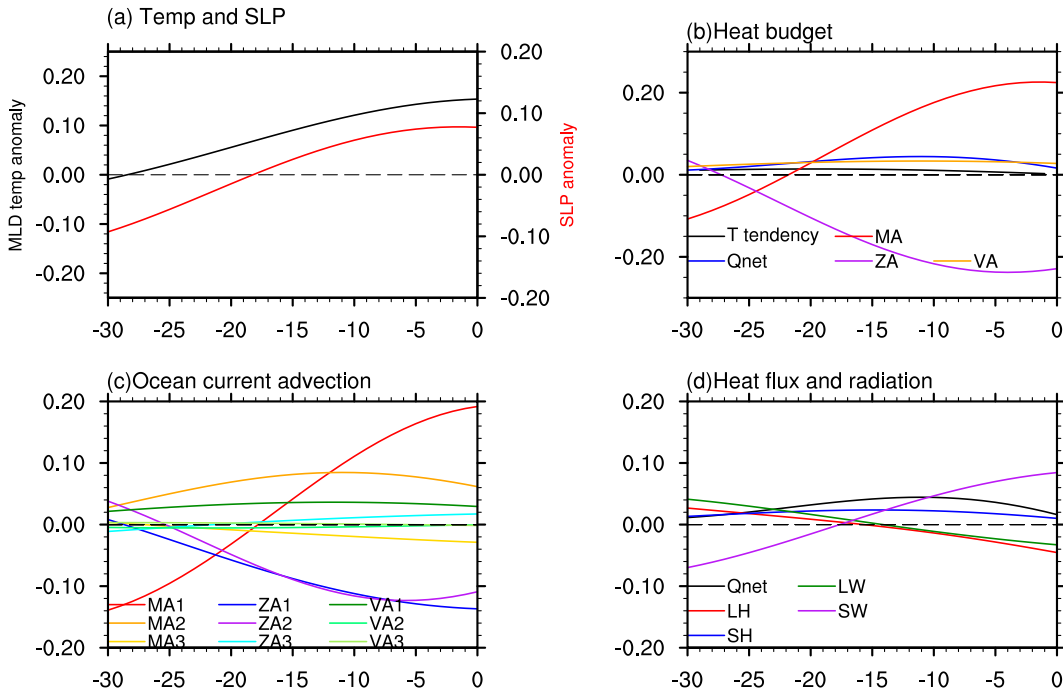


FIG. 11. As in Fig. 10, but for GFDL-CM4. These anomalies are obtained by regressing onto the multidecadal-filtered SWIOI as the SWIOI lags from 30 to 0 years and then averaged over the SWIO.

growth rate that is defined as  $\sigma_{BI} = 0.31f|\partial\mathbf{V}/\partial z|/N$ , where  $\mathbf{V}$  denotes the horizontal wind and  $N$  is the Brunt-Väisälä frequency (Lindzen and Farrell 1980; Hoskins and Valdes 1990).

Furthermore, for assessing the contribution from synoptic eddy to the tendency anomalies in geopotential height and westerly mean flow, the transient eddy vorticity forcing

( $F_{\text{eddy}}$ ) determined by the convergence of vorticity flux transport by transient eddies and the divergence of the horizontal Eliassen-Palm flux ( $\nabla \cdot \mathbf{E}$ ) are analyzed:

$$F_{\text{eddy}} = -\frac{f}{g} \cdot \nabla^{-2} [\overline{\nabla \cdot (\mathbf{V}'\zeta')}], \quad (4)$$

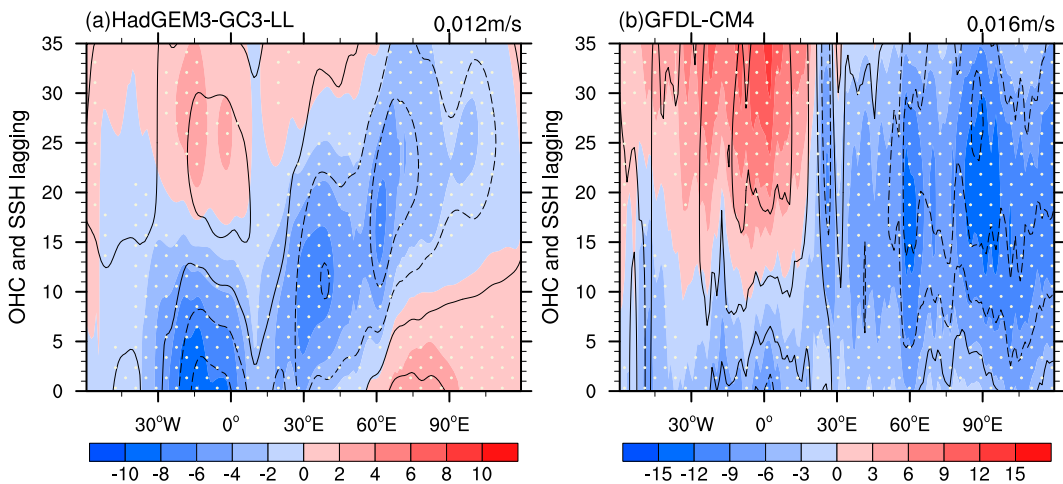


FIG. 12. Regression maps of annual mean ocean heat content (OHC; shaded;  $10^4 \text{ J m}^{-2}$ ) in the top 500 m and sea surface height (SSH; contour; m) meridionally averaged over  $55^\circ\text{--}40^\circ\text{S}$  at different lags from 0 to 35 years onto the multidecadal-filtered AMOC\_SF in (a) HadGEM3-GC3.1-LL. (b) As in (a), but for GFDL-CM4. Estimated propagation speed of the OHC is displayed at the top right of each panel. The stippling indicates the anomalies exceeding the 95% confidence level.

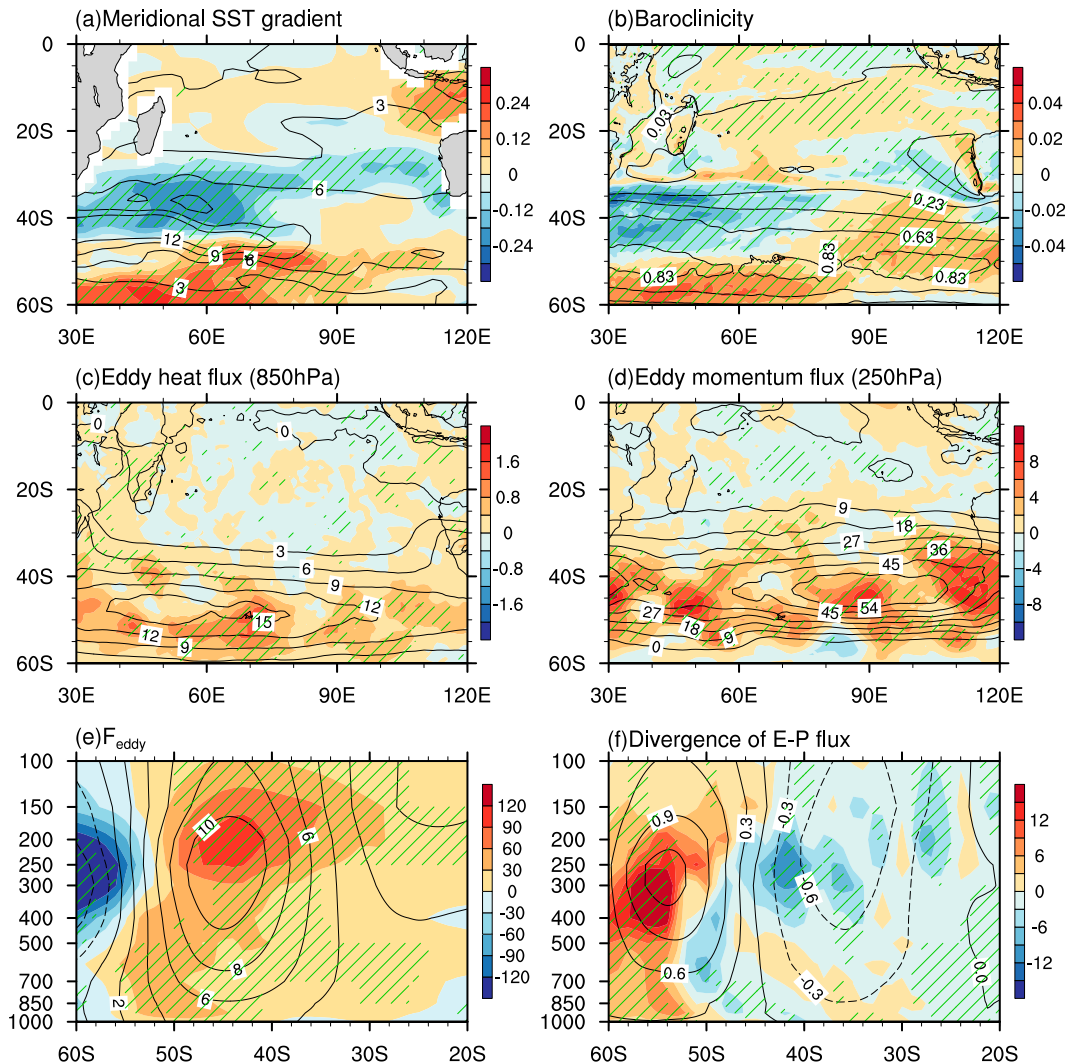


FIG. 13. Regression maps of (a) meridional SST gradient (shaded;  $10^{-6} \text{ }^{\circ}\text{C m}^{-1}$ ), (b) baroclinicity (shaded;  $\text{day}^{-1}$ ), (c) transient eddy heat flux at 850 hPa (shaded;  $^{\circ}\text{C m s}^{-1}$ ), (d) transient eddy momentum flux at 250 hPa (shaded;  $\text{m}^{-2} \text{ s}^{-2}$ ), (e)  $F_{\text{eddy}}$  (shaded;  $\text{m month}^{-1}$ ), and (f)  $\nabla \cdot E$  (shaded;  $\text{m s}^{-1} \text{ month}^{-1}$ ) zonally averaged over ( $40^{\circ}$ – $75^{\circ}\text{E}$ ) in DJF onto the multidecadal-filtered SWIOI based on observations/reanalysis. The contours in (a)–(d) represent their climatological values and in (e) and (f) the contours represent the regressions of zonally averaged geopotential height and zonal wind over  $40^{\circ}$ – $75^{\circ}\text{E}$  in DJF onto the multidecadal-filtered SWIOI. The green shading indicates the anomaly exceeding the 95% confidence level.

$$E = \left[ \frac{1}{2}(\overline{v^2} - \overline{u^2}), -\overline{u'v'} \right]. \quad (5)$$

Here,  $\mathbf{V}$  is the horizontal wind vector,  $\zeta$  represents the relative vorticity, and  $u$  and  $v$  are the horizontal winds. The divergence (convergence) of  $E$  indicates an increase (decrease) in the climatological westerlies.

For observations (Fig. 13), the climatological oceanic front is located between  $40^{\circ}$  and  $45^{\circ}\text{S}$  in the midlatitude SIO, accompanied by strong low-tropospheric baroclinicity and associated active storm tracks (Figs. 13a–c). Corresponding to the positive SST anomaly in the SWIO, the anomalous SST meridional gradient at midlatitude displays a dipole-like pattern, with positive (negative) anomaly on the poleward

(equatorward) flank of the climatological maximum, suggesting the poleward shift and intensification of the climatological oceanic front (Fig. 13a). As a response to the dipole-like pattern of the gradient anomaly, the baroclinicity in the lower troposphere also exhibits a meridional dipole structure, significantly enhanced (reduced) to the south (north) of the center of mean-state baroclinicity. The enhancement of the baroclinicity leads to a coherent strengthening of the transient eddy activities in the south of the climatological storm track in both the lower and upper troposphere (Figs. 13c,d). However, in spite of the large negative baroclinicity anomaly emerging to the north of the oceanic front, the local storm activities do not show the corresponding change. This geographically asymmetric response of the storm track presumably results from

the different sensitivity of the storm track to the latitudinal location of the SST gradient anomaly; that is, when the SST gradient is close to the subtropical jet, it will have a stronger impact on the storm tracks (Brayshaw et al. 2008; Zhang et al. 2021). To further explore the effect of the synoptic eddies on the geopotential height, the pressure–latitude section of the regressed  $F_{\text{eddy}}$  averaged between 40° and 75°E is illustrated (Fig. 13e). The  $F_{\text{eddy}}$  anomalies are featured as positive anomalies in the upper troposphere over the SWIO between 50° and 40°S and negative anomalies are around 60°S, displaying an equivalent barotropic structure with maxima at 200 and 250 hPa, respectively (Fig. 13e). This vertical distribution is nearly in phase with the geopotential height anomaly (Fig. 13e). These results suggest that the anomalous meridional SST gradient induced by the positive SST anomaly in the SWIO acts to cause the storm track in the lower and upper troposphere to shift poleward, thereby producing an equivalent barotropic pressure anomaly via the vorticity forcing from synoptic eddies. Moreover, with the close relationship between the storm track variation and westerly jet based on the eddy–mean flow interaction, the effect of anomalous transient eddies on the westerlies is also investigated. According to Fig. 13f, anomalous divergence (convergence) of  $E$  can be observed at 60°–50°S (45°–30°S) and it is in phase with the zonal wind anomalies, which indicates the roles of transient eddies in enhancing (reducing) the westerlies. Despite the contribution of the transient eddies, about 37.2% of the zonal wind anomaly is contributed by the meridional gradient of the air temperature based on the thermal wind balance (figure not shown). Similar mechanisms are also evident in the model simulations (Figs. S8 and S9). Interestingly, contrary to the nonsignificantly negative anomalies of eddy activities responding to the decreased SST gradient and baroclinicity over the north flank of positive SST anomalies, the reduced eddy activities are obvious in the model simulations (Figs. S8c,d and S9c,d). The symmetry of the storm track response to the SST anomaly in SWIO and the reason for this discrepancy between observations and models need further investigation.

As discussed in section 4, as atmospheric anomalies establish over the SWIO, it will amplify the multidecadal SST anomalies in the SWIO by modulating the air–sea heat exchange and oceanic meridional advection. The effect of the MA1 is robust in both model simulations and observations (Figs. 10c and 11c and Fig. S7b). Although the  $Q_{\text{net}}$  shows a significant effect on enhancing the multidecadal SST anomalies in the SWIO, the magnitude of each component varies among models and observations. The LH contribution is slightly larger than the other terms in HadGEM3-GC3.1-LL, the SH and SW seem to be more important in GFDL-CM4, and the LH and SH are predominant in the observations. Nonetheless, the local air–sea positive feedback exists in both observations and model simulations and presents an influential role in the multidecadal variability of the air–sea coupling system in the SWIO.

## 6. Discussion

As mentioned above, only 2 of 10 models can capture the relationship between AMOC and SWIOI shown in observations. It is also worthwhile to investigate the possible reasons

for their poor relationship in other models. According to the above analysis, the eastward propagation of SST anomalies from the SA associated with the AMOC variation is the key process to link the AMOC and SWIO multidecadal variability. Many studies have demonstrated that the enhanced AMOC will lead to a cooler SA and a warmer NA by modulating the meridional oceanic heat transport (OHT) (Latif et al. 2006; Dima and Lohmann 2010; Sun et al. 2018, 2021). In the Atlantic, OHT is northward everywhere and peaks at 20°N and the positive phase of the AMOC leads to the strengthening of the northward OHT with anomalous divergence in the SA leading to local cooling (Buckley and Marshall 2016). However, unlike consistent positive correlations between AMOC\_SF and SST variation in the NA pole among different models, negative correlations between AMOC and SST in the SA pole show distinct features. Six models showing the negative relationship between AMOC\_SF and SST in the SA pole, while only three of them (GFDL-CM4, HadGEM3-GC3.1-LL, and MIROC6) have a correlation above  $-0.25$  (Table 1). Some models, like ACCESS-CM2, FGOALS-g3, and MRI-ESM2-0, even show weak positive correlations (Table 1). According to the OHC anomalies in the upper 500 m associated with the positive phase of AMOC multidecadal variation, the exact location of the strongest cooling in the SA varies across models (Fig. 14). Most models show the cooling in the large region to the south of the equator (CanESM5, CESM2, GFDL-CM4, GISS-ES-1-G, HadGEM3-GC3.1-LL, and MIROC6), but only GFDL-CM4 and HadGEM3-GC3.1-LL have the strongest cooling at midlatitudes in the Southern Hemisphere (Fig. 14). The correlation between the AMOC\_SF index and the OHC in the top 500 m over the SA can reach  $-0.46$  (GFDL-CM4) and  $-0.52$  (HadGEM3-GC3.1-LL). Other models (ACCESS-CM2, FGOALS-g3, and MRI-ESM2-0) only show the cooling at low latitudes. These results imply that the sufficiently strong temperature anomalies related to the AMOC variation in the SA pole are important for the AMOC influencing SST variation in the SWIO.

The variable distributions of the OHC anomalies over the South Atlantic associated with AMOC among different models (Fig. 14) result from the different advection of mean meridional temperature by anomalous currents. For those models in which the SA shows cooling (Figs. 14c,f,g,h), the negative meridional advection associated with the current anomalies in the top 500 m (MA500) appears in the SA (Figs. 15c,f,g,h), with the strongest negative MA500 anomalies occurring in HadGEM3-GC3.1-LL and GFDL-CM4 (Figs. 15f,h), which is consistent with the most significant cooling over the SA in these two models (Figs. 14f,h). Some other models, which present weak warming in the SA (Figs. 14a,e,j), show weak positive MA500 anomalies in the SA (Figs. 15a,e,j). Meanwhile, the different OHC anomalies in the subtropical South Atlantic between GFDL-CM4 and HadGEM3-GC3.1-LL may also result from changes in MA500. Unlike the strong negative MA500 anomalies in the subtropical South Atlantic in HadGEM3-GC3.1-LL (Fig. 15h), there are weak positive MA500 anomalies there in GFDL-CM4 (Fig. 15f). Although the results suggest the important role of the AMOC-related meridional advection on the oceanic temperature in the SA, these discrepancies among model simulations require further investigation.

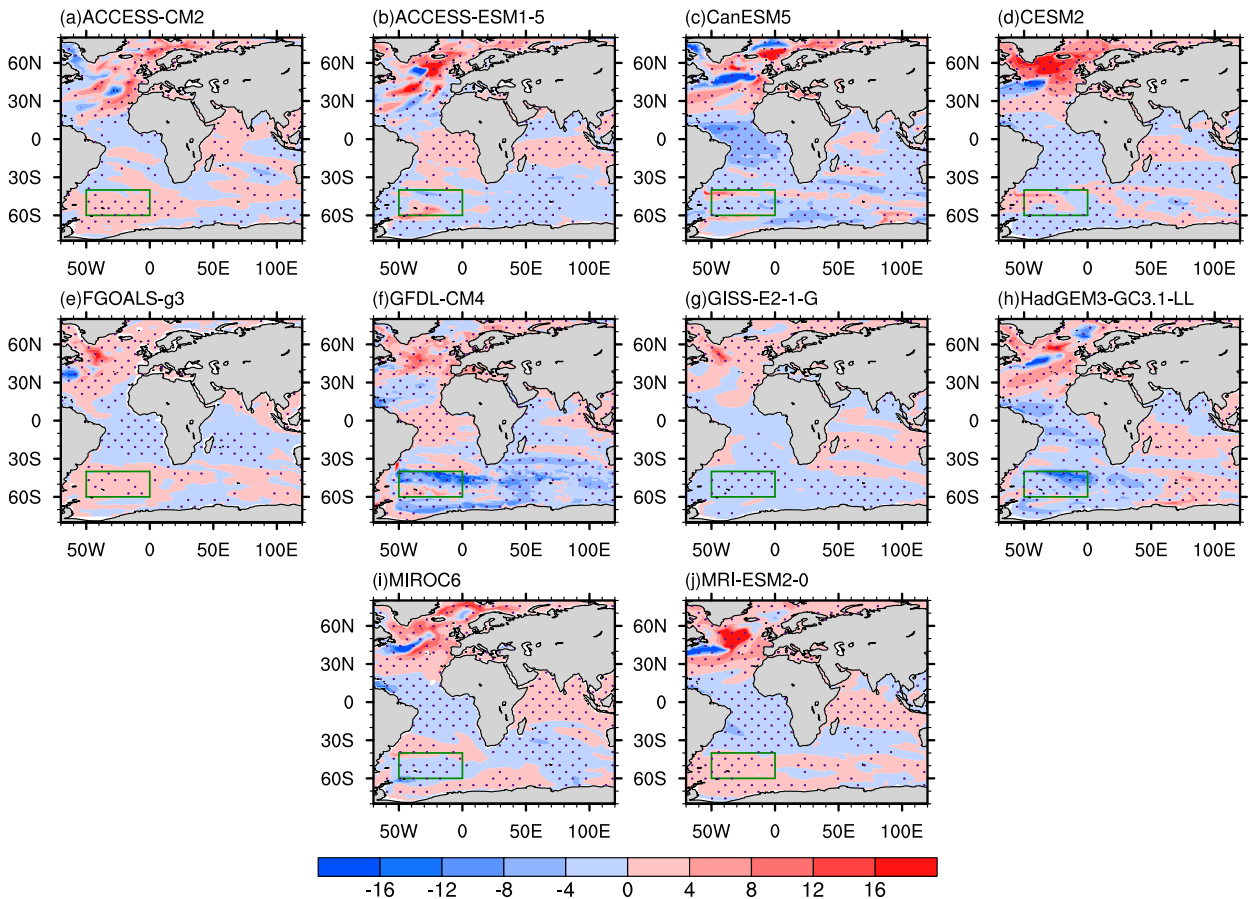


FIG. 14. Regressed OHC ( $10^4 \text{ J m}^{-2}$ ) in the upper 500 m onto the multidecadal-filtered AMOC\_SF in the CMIP6 model preindustrial simulations when the OHC lags. The lag year of each model is shown in Table 1. The stippling indicates the anomalies exceeding the 95% confidence level. The green box denotes the SA pole, covering  $40^\circ\text{--}60^\circ\text{S}$ ,  $50^\circ\text{W}\text{--}0^\circ$ .

But how does the multidecadal variability in the SWIO form in those models where the AMOC cannot affect the SWIO—especially for FGOALS-g3, MIROC6, and MRI-ESM2-0, in which the period of the AMOC\_SF and SWIOI has a good resemblance? To address this question, the lead and lag correlations between SLPI and SWIOI are investigated (Fig. S10). For observations/reanalysis and GFDL-CM4 model, the maximum positive correlation appears when the SWIOI leads by several years, and HadGEM3-GC3.1-LL shows the largest simultaneous correlation. In contrast, for the other three models, the highest correlations occur when SLPI leads by several years. This suggests that the multidecadal variability of the SWIO in these models may be first triggered by atmospheric forcing. The slow changes of the subsequent SST can be explained as the integral response of ocean to continuous random atmospheric forcing and air–sea coupling appears to modify the amplitude of the variability (Hasselmann 1976; Power et al. 1995; Delworth and Greatbatch 2000).

## 7. Conclusions

The characteristics and formation processes of the low-frequency variability of the air–sea coupling system in the SWIO

were investigated in this study. The results indicate that the SST and atmospheric circulation present significant multidecadal variability in the SWIO, where the Agulhas Current system is located and the local air–sea interaction is intense. This multidecadal anomaly of the air–sea coupling system is strongest during the austral summer and characterized by an equivalent barotropic atmospheric high (low) pressure over a warm (cold) SST and a poleward (equatorward) shift of the westerly wind band during the SWIO positive (negative) phase.

The schematic diagram depicting the mechanisms responsible for the formation of the multidecadal variability in the SWIO is shown in Fig. 16. It is found that the preceding AMOC has a pronounced effect on the multidecadal SST variability in the SWIO. They present a markedly negative correlation when the AMOC is leading by about a decade, which was demonstrated by both observational analysis and CMIP6 models (HadGEM3-GC3.1-LL and GFDL-CM4). The AMOC variation can lead to a dipole pattern of SST anomalies in the midlatitudes over the Atlantic Ocean through changing the meridional heat transport, and the anomalies in the SA propagate to the SWIO. Although anomalous zonal temperature advection by mean zonal current plays some role in the eastward propagating temperature anomalies, this propagation shows a

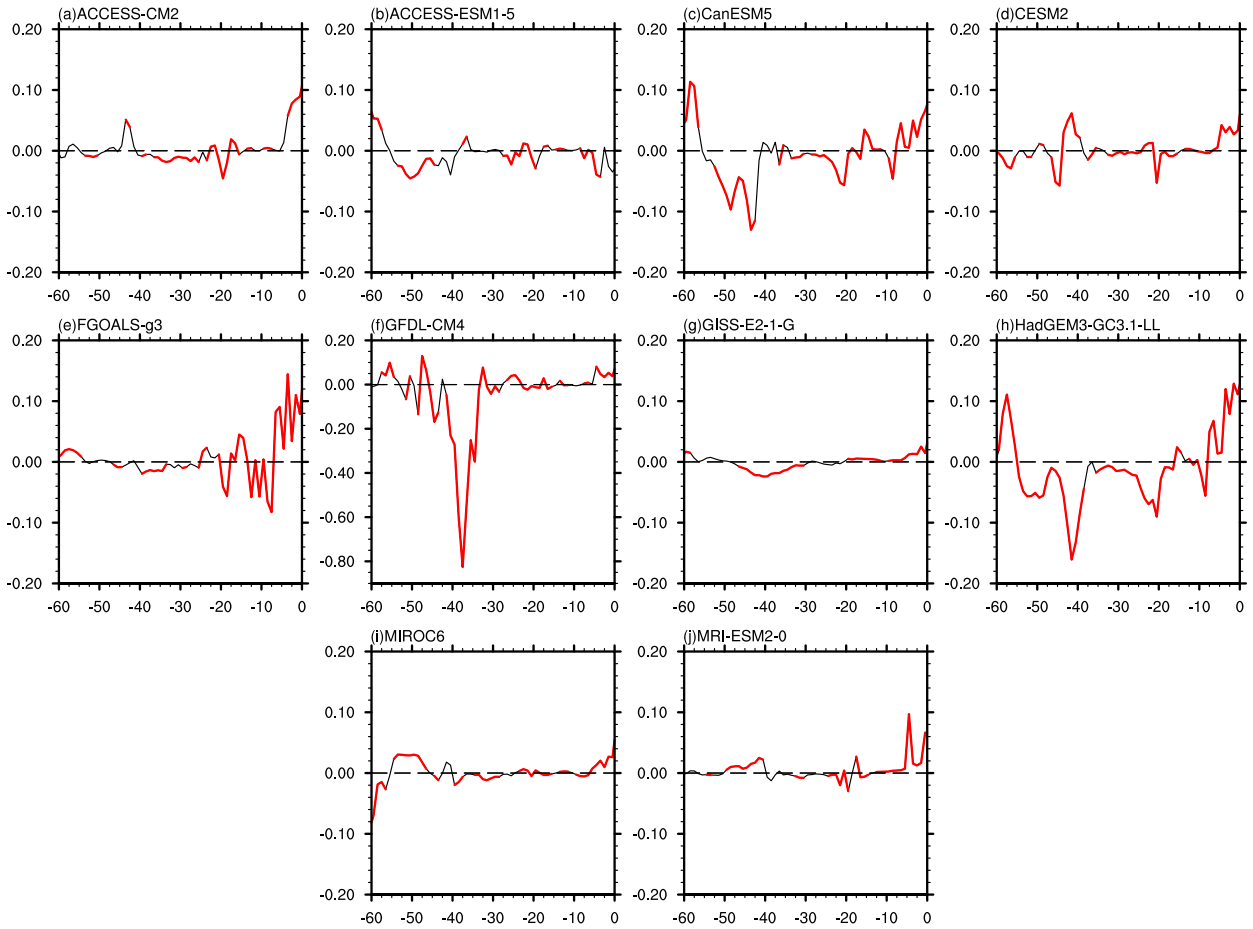


FIG. 15. Regressed meridional temperature advection associated with the current anomalies ( $^{\circ}\text{C yr}^{-1}$ ) averaged at  $70^{\circ}\text{W}$ – $20^{\circ}\text{E}$  in the upper 500 m of the South Atlantic onto the multidecadal-filtered AMOC\_SF index in the CMIP6 model preindustrial simulations when the temperature advection lags. The lag year of each model is shown in Table 1. The red lines denote the anomalies passing the 95% confidence level.

slower speed than the mean zonal current. According to the evolution of the SSH that is fairly similar to the SST, this eastward propagation of the SST may be mainly attributed to the ocean Rossby wave driven by the ACC.

In addition, the local air–sea positive feedback plays an important role in maintaining and strengthening this multidecadal variability in the SWIO. Once the SST anomalies associated with the AMOC multidecadal variation reach the SWIO, the

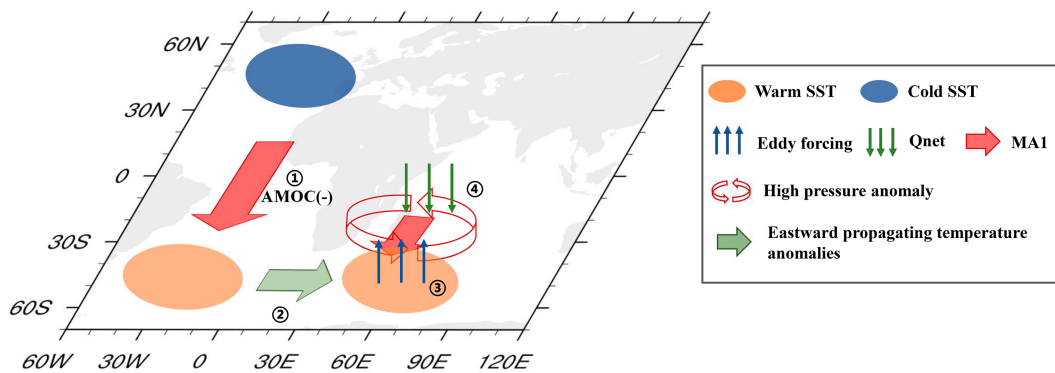


FIG. 16. Schematic diagram describing the possible formation processes of multidecadal variability of the air–sea coupling system in the SWIO associated with negative phase of AMOC.

corresponding pressure anomaly will be generated through changes in transient eddy activities induced by changes in the lower tropospheric baroclinicity related to changes in the meridional SST gradient. This pressure anomaly will further amplify the underneath SST anomalies through the local air–sea positive feedback by changes in the net surface heat flux and the meridional temperature advection. When the SWIO is dominated by a high pressure anomaly, the decreased westerlies caused by the easterlies in the north flank of the high pressure anomaly lead to less latent and sensible heat loss from the ocean. Besides, the anomalous southward current driven by the anomalous northerlies in the west flank of the high pressure anomaly causes the stronger southward temperature advection, reinforcing the warming in the SWIO.

However, we also noted that some other models fail to capture the negative correlation between the AMOC and multidecadal SST variations in the SWIO, which may be due to their weak SST anomalies and the nonsignificant AMOC-related meridional temperature advection in the SA. In these models that show a poor relationship between AMOC and SWIO SST, the integral response of the ocean to continuous random atmospheric forcing may be more important for forming the multidecadal SST anomalies in the SWIO. The discrepancy in the AMOC-related meridional temperature advection among CMIP6 models is worth further study. Besides, the possible impacts of the multidecadal variability of the air–sea coupling system in the SWIO also need exploration in the future.

*Acknowledgments.* The authors thank Dr. Yanke Tan, Dr. Ruifen Zhan, Dr. Jiacan Yuan, Dr. Changlin Chen, and Dr. Zhenqiang Zhou for their valuable suggestions. The author is also grateful to three anonymous reviewers providing constructive comments to improve the manuscript. This research was jointly supported by the National Key Research and Development Program of China (2022YFF0801701) and National Natural Science Foundation of China (42030601 and 41905072). Ruijie Zhang was supported by China Scholarship Council. Buwen Dong was supported by the U.K. National Centre for Atmospheric Science at the University of Reading.

*Data availability statement.* The fifth generation of the global European Centre for Medium-Range Weather Forecasts (ECMWF) atmospheric reanalysis (ERA5) is available at <https://cds.climate.copernicus.eu#!/search?text=ERA5&type=dataset>. Sea surface temperature (SST) in this study is derived from the National Oceanic and Atmospheric Administration (NOAA) at <https://psl.noaa.gov/data/gridded/data.noaa.ersst.v5.html>. The oceanic temperature and currents of the UMD Simple Ocean Data Assimilation Reanalysis Version 2.2.4 (SODA 2.2.4) are from the website at [http://apdrc.soest.hawaii.edu/datadoc/soda\\_2.2.4.php](http://apdrc.soest.hawaii.edu/datadoc/soda_2.2.4.php). The oceanic mixed layer depth of NCEP Global Ocean Data Assimilation System (GODAS) is available at <https://www.psl.noaa.gov/data/gridded/data.godas.html>, and AMOC streamfunction profiles from the RAPID array across the Atlantic at 26°N are from [https://rapid.ac.uk/rapidmoc/rapid\\_data/datadl.php](https://rapid.ac.uk/rapidmoc/rapid_data/datadl.php). The monthly outputs of

preindustrial control (piControl) simulations from 10 models from phase 6 of the Coupled Model Intercomparison Project (CMIP6) are openly available at <https://esgf-node.lnl.gov/projects/cmip6/>.

## REFERENCES

- Allan, R. J., J. A. Lindesay, and C. J. C. Reason, 1995: Multidecadal variability in the climate system over the Indian Ocean region during the austral summer. *J. Climate*, **8**, 1853–1873, [https://doi.org/10.1175/1520-0442\(1995\)008<1853:MVITCS>2.0.CO;2](https://doi.org/10.1175/1520-0442(1995)008<1853:MVITCS>2.0.CO;2).
- Behringer, D. W., M. Ji, and A. Leetmaa, 1998: An improved coupled model for ENSO prediction and implications for ocean initialization. Part I: The ocean data assimilation system. *Mon. Wea. Rev.*, **126**, 1013–1021, [https://doi.org/10.1175/1520-0493\(1998\)126<1013:AICMFE>2.0.CO;2](https://doi.org/10.1175/1520-0493(1998)126<1013:AICMFE>2.0.CO;2).
- Bell, B., and Coauthors, 2020: ERA5 monthly averaged data on single levels from 1950 to 1978 (preliminary version). Copernicus Climate Change Service (C3S) Climate Data Store (CDS), accessed 6 January 2021, <https://cds.climate.copernicus.eu/cdsapp#!/dataset/reanalysis-era5-single-levels-monthly-means-preliminary-back-extension?tab=doc>.
- Brayshaw, D. J., B. Hoskins, and M. Blackburn, 2008: The storm-track response to idealized SST perturbations in an aquaplanet GCM. *J. Atmos. Sci.*, **65**, 2842–2860, <https://doi.org/10.1175/2008JAS2657.1>.
- Buckley, M. W., and J. Marshall, 2016: Observations, inferences, and mechanisms of the Atlantic meridional overturning circulation: A review. *Rev. Geophys.*, **54**, 5–63, <https://doi.org/10.1002/2015RG000493>.
- Carton, J. A., and B. S. Giese, 2008: A reanalysis of ocean climate using Simple Ocean Data Assimilation (SODA). *Mon. Wea. Rev.*, **136**, 2999–3017, <https://doi.org/10.1175/2007MWR1978.1>.
- , —, and S. A. Grodsky, 2005: Sea level rise and the warming of the oceans in the Simple Ocean Data Assimilation (SODA) ocean reanalysis. *J. Geophys. Res.*, **110**, C09006, <https://doi.org/10.1029/2004JC002817>.
- Cayan, D. R., 1992: Latent and sensible heat flux anomalies over the northern oceans: The connection to monthly atmospheric circulation. *J. Climate*, **5**, 354–369, [https://doi.org/10.1175/1520-0442\(1992\)005<0354:LASHFA>2.0.CO;2](https://doi.org/10.1175/1520-0442(1992)005<0354:LASHFA>2.0.CO;2).
- Chelton, D. B., and M. G. Schlax, 1996: Global observation of oceanic Rossby waves. *Science*, **272**, 234–238, <https://doi.org/10.1126/science.272.5259.234>.
- Chen, L., J. Fang, and X.-Q. Yang, 2020: Midlatitude unstable air–sea interaction with atmospheric transient eddy dynamical forcing in an analytical coupled model. *Climate Dyn.*, **55**, 2557–2577, <https://doi.org/10.1007/s00382-020-05405-0>.
- Chidichimo, M. P., and Coauthors, 2023: Energetic overturning flows, dynamic interocean exchanges, and ocean warming observed in the South Atlantic. *Commun. Earth Environ.*, **4**, 10, <https://doi.org/10.1038/s43247-022-00644-x>.
- Cipollini, P., D. Cromwell, P. G. Challenor, and S. Raffaglio, 2001: Rossby waves detected in global ocean colour data. *Geophys. Res. Lett.*, **28**, 323–326, <https://doi.org/10.1029/1999GL011231>.
- Delworth, T. L., and R. J. Greatbatch, 2000: Multidecadal thermohaline circulation variability driven by atmospheric surface flux forcing. *J. Climate*, **13**, 1481–1495, [https://doi.org/10.1175/1520-0442\(2000\)013<1481:MTCVDB>2.0.CO;2](https://doi.org/10.1175/1520-0442(2000)013<1481:MTCVDB>2.0.CO;2).

- Deser, C., R. A. Tomas, and S. Peng, 2007: The transient atmospheric circulation response to North Atlantic SST and sea ice anomalies. *J. Climate*, **20**, 4751–4767, <https://doi.org/10.1175/JCLI4278.1>.
- Dima, M., and G. Lohmann, 2010: Evidence for two distinct modes of large-scale ocean circulation changes over the last century. *J. Climate*, **23**, 5–16, <https://doi.org/10.1175/2009JCLI2867.1>.
- Eyring, V., S. Bony, G. A. Meehl, C. A. Senior, B. Stevens, R. J. Stouffer, and K. E. Taylor, 2016: Overview of the Coupled Model Intercomparison Project Phase 6 (CMIP6) experimental design and organization. *Geosci. Model Dev.*, **9**, 1937–1958, <https://doi.org/10.5194/gmd-9-1937-2016>.
- Fang, J.-B., and X.-Q. Yang, 2011: The relative roles of different physical processes in unstable midlatitude ocean–atmosphere interactions. *J. Climate*, **24**, 1542–1558, <https://doi.org/10.1175/2010JCLI3618.1>.
- , and —, 2016: Structure and dynamics of decadal anomalies in the wintertime midlatitude North Pacific ocean–atmosphere system. *Climate Dyn.*, **47**, 1989–2007, <https://doi.org/10.1007/s00382-015-2946-x>.
- Feng, M., M. J. McPhaden, S.-P. Xie, and J. Hafner, 2013: La Niña forces unprecedented Leeuwin Current warming in 2011. *Sci. Rep.*, **3**, 1277, <https://doi.org/10.1038/srep01277>.
- Gao, X., Y. Li, P. Lin, L. Zhang, Q. Ren, Y. Lu, and F. Wang, 2023: Origins of multidecadal SST variations in the southern Atlantic and Indian Oceans since the 1960s. *Geophys. Res. Lett.*, **50**, e2022GL101735, <https://doi.org/10.1029/2022GL101735>.
- Hasselmann, K., 1976: Stochastic climate models Part I. Theory. *Tellus*, **28**, 473–485, <https://doi.org/10.1111/j.2153-3490.1976.tb00696.x>.
- Hersbach, H., and Coauthors, 2018: ERA5 hourly data on pressure levels from 1959 to present. Copernicus Climate Change Service (C3S) Climate Data Store (CDS), accessed 6 January 2021, <https://doi.org/10.24381/cds.bd0915c6>.
- , and Coauthors, 2019a: ERA5 monthly averaged data on single levels from 1959 to present. Copernicus Climate Change Service (C3S) Climate Data Store (CDS), accessed 6 January 2021, <https://doi.org/10.24381/cds.f17050d7>.
- , and Coauthors, 2019b: ERA5 monthly averaged data on pressure levels from 1959 to present. Copernicus Climate Change Service (C3S) Climate Data Store (CDS), accessed 6 January 2021, <https://doi.org/10.24381/cds.6860a573>.
- Hogg, A. M. C., and J. R. Blundell, 2006: Interdecadal variability of the Southern Ocean. *J. Phys. Oceanogr.*, **36**, 1626–1645, <https://doi.org/10.1175/JPO2934.1>.
- Hoskins, B. J., and P. J. Valdes, 1990: On the existence of stormtracks. *J. Atmos. Sci.*, **47**, 1854–1864, [https://doi.org/10.1175/1520-0469\(1990\)047<1854:OTEOST>2.0.CO;2](https://doi.org/10.1175/1520-0469(1990)047<1854:OTEOST>2.0.CO;2).
- Huang, B., and Coauthors, 2017: Extended Reconstructed Sea Surface Temperature, version 5 (ERSSTv5): Upgrades, validations, and intercomparisons. *J. Climate*, **30**, 8179–8205, <https://doi.org/10.1175/JCLI-D-16-0836.1>.
- Hughes, C. W., 1996: The Antarctic Circumpolar Current as a waveguide for Rossby waves. *J. Phys. Oceanogr.*, **26**, 1375–1387, [https://doi.org/10.1175/1520-0485\(1996\)026<1375:TACCAA>2.0.CO;2](https://doi.org/10.1175/1520-0485(1996)026<1375:TACCAA>2.0.CO;2).
- Jin, F.-F., S. T. Kim, and L. Bejarano, 2006: A coupled-stability index for ENSO. *Geophys. Res. Lett.*, **33**, L23708, <https://doi.org/10.1029/2006GL027221>.
- Jury, M. R., 2015: Factors contributing to a decadal oscillation in South African rainfall. *Theor. Appl. Climatol.*, **120**, 227–237, <https://doi.org/10.1007/s00704-014-1165-4>.
- Kerr, R. A., 2000: A North Atlantic climate pacemaker for the centuries. *Science*, **288**, 1984–1986, <https://doi.org/10.1126/science.288.5473.1984>.
- Kushnir, Y., W. A. Robinson, I. Bladé, N. M. J. Hall, S. Peng, and R. Sutton, 2002: Atmospheric GCM response to extratropical SST anomalies: Synthesis and evaluation. *J. Climate*, **15**, 2233–2256, [https://doi.org/10.1175/1520-0442\(2002\)015<2233:AGRITES>2.0.CO;2](https://doi.org/10.1175/1520-0442(2002)015<2233:AGRITES>2.0.CO;2).
- Latif, M., and T. P. Barnett, 1994: Causes of decadal climate variability over the North Pacific and North America. *Science*, **266**, 634–637, <https://doi.org/10.1126/science.266.5185.634>.
- , and Coauthors, 2004: Reconstructing, monitoring, and predicting multidecadal-scale changes in the North Atlantic thermohaline circulation with sea surface temperature. *J. Climate*, **17**, 1605–1614, [https://doi.org/10.1175/1520-0442\(2004\)017<1605:RMAPMC>2.0.CO;2](https://doi.org/10.1175/1520-0442(2004)017<1605:RMAPMC>2.0.CO;2).
- , C. Böning, J. Willebrand, A. Biastoch, J. Dengg, N. Keenlyside, U. Schwecjendiek, and G. Madec, 2006: Is the thermohaline circulation changing? *J. Climate*, **19**, 4631–4637, <https://doi.org/10.1175/JCLI3876.1>.
- Le Bars, D., J. P. Viebahn, and H. A. Dijkstra, 2016: A Southern Ocean mode of multidecadal variability. *Geophys. Res. Lett.*, **43**, 2102–2110, <https://doi.org/10.1002/2016GL068177>.
- Li, J., and J. Su, 2021: Sustained decadal warming phase in the southwestern Indian Ocean since the mid-1990s. *J. Meteor. Res.*, **35**, 258–270, <https://doi.org/10.1007/s13351-021-0112-4>.
- Li, X., D. M. Holland, E. P. Gerber, and C. Yoo, 2014: Impacts of the north and tropical Atlantic Ocean on the Antarctic Peninsula and sea ice. *Nature*, **505**, 538–542, <https://doi.org/10.1038/nature12945>.
- Lindzen, R. S., and B. Farrell, 1980: A simple approximate result for the maximum growth rate of baroclinic instabilities. *J. Atmos. Sci.*, **37**, 1648–1654, [https://doi.org/10.1175/1520-0469\(1980\)037<1648:ASARFT>2.0.CO;2](https://doi.org/10.1175/1520-0469(1980)037<1648:ASARFT>2.0.CO;2).
- Liu, Q.-Y., M. Feng, D. Wang, and S. Wijffels, 2015: Interannual variability of the Indonesian Throughflow transport: A revisit based on 30 year expendable bathythermograph data. *J. Geophys. Res. Oceans*, **120**, 8270–8282, <https://doi.org/10.1002/2015JC011351>.
- Liu, Z., and L. Wu, 2004: Atmospheric response to North Pacific SST: The role of ocean–atmosphere coupling. *J. Climate*, **17**, 1859–1882, [https://doi.org/10.1175/1520-0442\(2004\)017<1859:ARTNPS>2.0.CO;2](https://doi.org/10.1175/1520-0442(2004)017<1859:ARTNPS>2.0.CO;2).
- Malherbe, J., W. A. Landman, and F. A. Engelbrecht, 2014: The bi-decadal rainfall cycle, southern annular mode and tropical cyclones over the Limpopo River Basin, southern Africa. *Climate Dyn.*, **42**, 3121–3138, <https://doi.org/10.1007/s00382-013-2027-y>.
- Miller, A. J., and N. Schneider, 2000: Interdecadal climate regime dynamics in the North Pacific Ocean: Theories, observations and ecosystem impacts. *Prog. Oceanogr.*, **47**, 355–379, [https://doi.org/10.1016/S0079-6611\(00\)00044-6](https://doi.org/10.1016/S0079-6611(00)00044-6).
- Morioka, Y., F. Engelbrecht, and S. K. Behera, 2015a: Potential sources of decadal climate variability over southern Africa. *J. Climate*, **28**, 8695–8709, <https://doi.org/10.1175/JCLI-D-15-0201.1>.
- , K. Takaya, S. K. Behera, and Y. Masumoto, 2015b: Local SST impacts on the summertime Mascarene high variability. *J. Climate*, **28**, 678–694, <https://doi.org/10.1175/JCLI-D-14-00133.1>.

- , B. Taguchi, and S. K. Behera, 2017: Eastward propagating decadal temperature variability in the South Atlantic and Indian Oceans. *J. Geophys. Res. Oceans*, **122**, 5611–5623, <https://doi.org/10.1002/2017JC012706>.
- Nakamura, H., T. Sampe, Y. Tanimoto, and A. Shimpo, 2004: Observed associations among storm tracks, jet streams and midlatitude oceanic fronts. *Earth's Climate: The Ocean–Atmosphere Interaction, Geophys. Monogr.*, Vol. 147, Amer. Geophys. Union, 329–345.
- , —, A. Goto, W. Ohfuchi, and S.-P. Xie, 2008: On the importance of midlatitude oceanic frontal zones for the mean state and dominant variability in the tropospheric circulation. *Geophys. Res. Lett.*, **35**, L15709, <https://doi.org/10.1029/2008GL034010>.
- Nakamura, M., 2012: Impacts of SST anomalies in the Agulhas Current system on the regional climate variability. *J. Climate*, **25**, 1213–1229, <https://doi.org/10.1175/JCLI-D-11-00088.1>.
- Nonaka, M., H. Nakamura, B. Taguchi, N. Komori, A. Kuwano-Yoshida, and K. Takaya, 2009: Air–sea heat exchanges characteristic of a prominent midlatitude oceanic front in the South Indian Ocean as simulated in a high-resolution coupled GCM. *J. Climate*, **22**, 6515–6535, <https://doi.org/10.1175/2009JCLI2960.1>.
- Ogawa, F., H. Nakamura, K. Nishii, T. Miyasaka, and A. Kuwano-Yoshida, 2016: Importance of midlatitude oceanic frontal zones for the annular mode variability: Interbasin differences in the southern annular mode signature. *J. Climate*, **29**, 6179–6199, <https://doi.org/10.1175/JCLI-D-15-0885.1>.
- Orihuela-Pinto, B., M. H. England, and A. S. Taschetto, 2022: Interbasin and interhemispheric impacts of a collapsed Atlantic overturning circulation. *Nat. Climate Change*, **12**, 558–565, <https://doi.org/10.1038/s41558-022-01380-y>.
- Power, S. B., F. Tseitkin, M. Dix, R. Kleeman, R. Colman, and D. Holland, 1995: Stochastic variability at the air–sea interface on decadal timescales. *Geophys. Res. Lett.*, **22**, 2593–2596, <https://doi.org/10.1029/95GL02655>.
- , —, V. Mehta, B. Lavery, S. J. Torok, and N. Holbrook, 1999: Decadal climate variability in Australia during the twentieth century. *Int. J. Climatol.*, **19**, 169–184, [https://doi.org/10.1002/\(SICI\)1097-0088\(199902\)19:2<169::AID-JOC356>3.0.CO;2-Y](https://doi.org/10.1002/(SICI)1097-0088(199902)19:2<169::AID-JOC356>3.0.CO;2-Y).
- Rayner, D., and Coauthors, 2011: Monitoring the Atlantic meridional overturning circulation. *Deep-Sea Res. II*, **58**, 1744–1753, <https://doi.org/10.1016/j.dsr2.2010.10.056>.
- Reason, C. J. C., 2001: Evidence for the influence of the Agulhas Current on regional atmospheric circulation patterns. *J. Climate*, **14**, 2769–2778, [https://doi.org/10.1175/1520-0442\(2001\)014<2769:EFTIOT>2.0.CO;2](https://doi.org/10.1175/1520-0442(2001)014<2769:EFTIOT>2.0.CO;2).
- , and J. R. E. Lutjeharms, 1998: Variability of the South Indian Ocean and implications for southern African rainfall. *S. Afr. J. Sci.*, **94**, 115–123, [https://hdl.handle.net/10520/AJA00382353\\_134](https://hdl.handle.net/10520/AJA00382353_134).
- , R. J. Allan, and J. A. Lindesay, 1996: Evidence for the influence of remote forcing on interdecadal variability in the southern Indian Ocean. *J. Geophys. Res.*, **101**, 11 867–11 882, <https://doi.org/10.1029/96JC00122>.
- Rouault, M., S. A. White, C. J. C. Reason, J. R. E. Lutjeharms, and I. Jobard, 2002: Ocean–atmosphere interaction in the Agulhas Current region and a South African extreme weather event. *Wea. Forecasting*, **17**, 655–669, [https://doi.org/10.1175/1520-0434\(2002\)017<0655:OAIITA>2.0.CO;2](https://doi.org/10.1175/1520-0434(2002)017<0655:OAIITA>2.0.CO;2).
- , C. J. C. Reason, J. R. E. Lutjeharms, and A. C. M. Beljaars, 2003: Underestimation of latent and sensible heat fluxes above the Agulhas Current in NCEP and ECMWF analyses. *J. Climate*, **16**, 776–782, [https://doi.org/10.1175/1520-0442\(2003\)016<0776:UOLASH>2.0.CO;2](https://doi.org/10.1175/1520-0442(2003)016<0776:UOLASH>2.0.CO;2).
- Ryan, S., C. C. Ummerhofer, G. Gawarkiewicz, P. Wagner, M. Scheinert, A. Biastoch, and C. W. Böning, 2021: Depth structure of Ningaloo Niño/Niña events and associated drivers. *J. Climate*, **34**, 1767–1788, <https://doi.org/10.1175/JCLI-D-19-1020.1>.
- Sampe, T., H. Nakamura, A. Goto, and W. Ohfuchi, 2010: Significance of a midlatitude SST frontal zone in the formation of a storm track and an eddy-driven westerly jet. *J. Climate*, **23**, 1793–1814, <https://doi.org/10.1175/2009JCLI3163.1>.
- Schmid, C., and S. Majumder, 2018: Transport variability of the Brazil Current from observations and a data assimilation model. *Ocean Sci.*, **14**, 417–436, <https://doi.org/10.5194/os-14-417-2018>.
- Seager, R., Y. Kushnir, N. H. Naik, M. A. Cane, and J. Miller, 2001: Wind-driven shifts in the latitude of the Kuroshio-Oyashio Extension and generation of SST anomalies on decadal timescales. *J. Climate*, **14**, 4249–4265, [https://doi.org/10.1175/1520-0442\(2001\)014<4249:WDSITL>2.0.CO;2](https://doi.org/10.1175/1520-0442(2001)014<4249:WDSITL>2.0.CO;2).
- Simpkins, G. R., S. McGregor, A. S. Taschetto, L. M. Ciasto, and M. H. England, 2014: Tropical connections to climatic change in the extratropical Southern Hemisphere: The role of Atlantic SST trends. *J. Climate*, **27**, 4923–4936, <https://doi.org/10.1175/JCLI-D-13-00615.1>.
- Stevenson, J. W., and P. P. Niiler, 1983: Upper ocean heat budget during the Hawaii-to-Tahiti shuttle experiment. *J. Phys. Oceanogr.*, **13**, 1894–1907, [https://doi.org/10.1175/1520-0485\(1983\)013<1894:UOHBDT>2.0.CO;2](https://doi.org/10.1175/1520-0485(1983)013<1894:UOHBDT>2.0.CO;2).
- Sun, C., J. Li, F.-F. Jin, and R. Ding, 2013: Sea surface temperature inter-hemispheric dipole and its relation to tropical precipitation. *Environ. Res. Lett.*, **8**, 044006, <https://doi.org/10.1088/1748-9326/8/4/044006>.
- , —, X. Li, J. Xue, R. Ding, F. Xie, and Y. Li, 2018: Oceanic forcing of the interhemispheric SST dipole associated with the Atlantic Multidecadal Oscillation. *Environ. Res. Lett.*, **13**, 074026, <https://doi.org/10.1088/1748-9326/aac666>.
- , J. Zhang, X. Li, C. Shi, Z. Gong, R. Ding, F. Xie, and P. Lou, 2021: Atlantic meridional overturning circulation reconstructions and instrumentally observed multidecadal climate variability: A comparison of indicators. *Int. J. Climatol.*, **41**, 763–778, <https://doi.org/10.1002/joc.6695>.
- Thompson, D. W. J., S. Solomon, P. J. Kushner, M. H. England, K. M. Grise, and D. J. Karoly, 2011: Signatures of the Antarctic ozone hole in Southern Hemisphere surface climate change. *Nat. Geosci.*, **4**, 741–749, <https://doi.org/10.1038/ngeo1296>.
- Vellinga, M., and R. A. Wood, 2002: Global climatic impacts of a collapse of the Atlantic thermohaline circulation. *Climatic Change*, **54**, 251–267, <https://doi.org/10.1023/A:1016168827653>.
- Venzke, S., M. Latif, and A. Villwock, 2000: The coupled GCM ECHO-2. Part II: Indian Ocean response to ENSO. *J. Climate*, **13**, 1371–1383, [https://doi.org/10.1175/1520-0442\(2000\)013<1371:TCGE>2.0.CO;2](https://doi.org/10.1175/1520-0442(2000)013<1371:TCGE>2.0.CO;2).
- Wallace, J. M., and Q. Jiang, 1987: On the observed structure of the interannual variability of the atmosphere/ocean climate system. *Atmospheric and Oceanic Variability*, H. Cattle, Ed., Royal Meteorological Society, 17–43.
- Xue, J., J. Li, C. Sun, S. Zhao, J. Mao, D. Dong, Y. Li, and J. Feng, 2018a: Decadal-scale teleconnection between South Atlantic SST and southeast Australia surface air temperature

- in austral summer. *Climate Dyn.*, **50**, 2687–2703, <https://doi.org/10.1007/s00382-017-3764-0>.
- , C. Sun, J. Li, and J. Mao, 2018b: South Atlantic forced multidecadal teleconnection to the midlatitude South Indian Ocean. *Geophys. Res. Lett.*, **45**, 8480–8489, <https://doi.org/10.1029/2018GL078990>.
- Zhang, L., B. Gan, L. Wu, W. Cai, and H. Ma, 2018: Seasonal dependence of coupling between storm tracks and sea surface temperature in the Southern Hemisphere midlatitudes: A statistical assessment. *J. Climate*, **31**, 4055–4074, <https://doi.org/10.1175/JCLI-D-17-0196.1>.
- , —, H. Wang, L. Wu, and W. Cai, 2020: Essential role of the midlatitude South Atlantic variability in altering the Southern Hemisphere summer storm tracks. *Geophys. Res. Lett.*, **47**, e2020GL087910, <https://doi.org/10.1029/2020GL087910>.
- , —, C.-Y. Wang, L. Wu, and W. Cai, 2021: Decadal coupling between storm tracks and sea surface temperature in the Southern Hemisphere midlatitudes. *Climate Dyn.*, **56**, 783–798, <https://doi.org/10.1007/s00382-020-05503-z>.
- Zhang, R., J. Fang, and X.-Q. Yang, 2020: What kinds of atmospheric anomalies drive wintertime North Pacific basin-scale subtropical oceanic front intensity variation? *J. Climate*, **33**, 7011–7026, <https://doi.org/10.1175/JCLI-D-19-0973.1>.
- , R. Sutton, G. Danabasoglu, Y. O. Kwon, R. Marsh, S. G. Yeager, D. E. Amrhein, and C. M. Little, 2019: A review of the role of the Atlantic meridional overturning circulation in Atlantic multidecadal variability and associated climate impacts. *Rev. Geophys.*, **57**, 316–375, <https://doi.org/10.1029/2019RG000644>.
- Zhang, Y., M. Feng, Y. Du, H. E. Phillips, N. L. Bindoff, and M. J. McPhaden, 2018: Strengthened Indonesian Throughflow drives decadal warming in the southern Indian Ocean. *Geophys. Res. Lett.*, **45**, 6167–6175, <https://doi.org/10.1029/2018GL078265>.
- Zhong, Y., Z. Liu, and R. Jacob, 2008: Origin of Pacific multidecadal variability in Community Climate System Model, version 3 (CCSM3): A combined statistical and dynamical assessment. *J. Climate*, **21**, 114–133, <https://doi.org/10.1175/2007JCLI1730.1>.
- Zhu, Z., J. Liu, M. Song, S. Wang, and Y. Hu, 2021: Impacts of Antarctic sea ice, AMV and IPO on extratropical Southern Hemisphere climate: A modeling study. *Front. Earth Sci.*, **9**, 757475, <https://doi.org/10.3389/feart.2021.757475>.